A&A 510, A86 (2010)
DOI: 10.1051/0004-6361/200913371


Astronomy & Astrophysics

# Looking for high-mass young stellar objects: $H_2O$ and OH masers in ammonia cores

C. Codella[1], R. Cesaroni[1], A. López-Sepulcre[1], M. T. Beltrán[1], R. Furuya[2], and L. Testi[1,3]

[1] INAF, Osservatorio Astrofisico di Arcetri, Largo E. Fermi 5, 50125 Firenze, Italy
e-mail: [codella;cesa;sepulcre;mbeltran;lt]@arcetri.astro.it
[2] Subaru Telescope, National Astronomical Observatory of Japan, 650 North A'ohoku Place, Hilo, HI 96720, USA
e-mail: rsf@subaru.naoj.org
[3] ESO, Karl Schwarzschild srt. 2, 85748 Garching, Germany
e-mail: ltesti@eso.org

Received 29 September 2009 / Accepted 5 November 2009

**ABSTRACT**

*Context.* The earliest stages of high-mass star formation have yet to be characterised well, because high-angular resolution observations are required to infer the properties of the molecular gas hosting the newly formed stars.
*Aims.* We search for high-mass molecular cores in a large sample of 15 high-mass star-forming regions that are observed at high-angular resolution, extending a pilot survey based on a smaller number of objects.
*Methods.* The sample was chosen from surveys of $H_2O$ and OH masers to favour the earliest phases of high-mass star formation. Each source was first observed with the 32-m single-dish Medicina antenna in the (1, 1) and (2, 2) inversion transitions at 1.3 cm of ammonia, which is an excellent tracer of dense gas. High-resolution maps in the $NH_3$(2, 2) and (3, 3) lines and the 1.3 cm continuum were obtained successively with the VLA interferometer.
*Results.* We detect continuum emission in almost all the observed star-forming regions, which corresponds to extended and UCHII regions created by young stellar objects with typical luminosities of $\sim 10^4$ $L_\odot$. However, only in three cases do we find a projected overlap between HII regions and $H_2O$ and OH maser spots. On the other hand, the VLA images detect eight ammonia cores closely associated with the maser sources. The ammonia cores have sizes of $\sim 10^4$ AU, and high masses (up to $10^4$ $M_\odot$), and are very dense (from $\sim 10^6$ to a few $\times 10^9$ cm$^{-3}$). The typical relative $NH_3$ abundance is $\leq 10^{-7}$, in agreement with previous measurements in high-mass star-forming regions.
*Conclusions.* The statistical analysis of the distribution between $H_2O$ and OH masers, $NH_3$ cores, and HII regions confirms that the earliest stages of high-mass star formation are characterised by high-density molecular cores with temperatures of on average $\geq$30 K, either without a detectable ionised region or associated with a hypercompact HII region.

**Key words.** stars: formation – stars: evolution – ISM: clouds – ISM: molecules – radio lines: ISM

## 1. Introduction

Understanding the process of high-mass (O-B type) star formation represents a challenge from both a theoretical and observational point of view. While low-mass stars are believed to form by means of accretion onto a protostar, more high-mass stars are expected to exert strong radiation pressure on the infalling gas, thus halting the accretion above $M_{\rm star} \simeq 8$ $M_\odot$ (Wolfire & Cassinelli 1987; Palla & Stahler 1993). To circumvent this theoretical problem, two alternative modes of high-mass star formation have been proposed (Stahler et al. 2000): (i) accretion at high rate across a thin disk; and (ii) coalescence of a dense cluster of lower mass stars (e.g., Bonnell & Bate 2005; Bonnell et al. 2007), although the controversy remains (e.g., Bonnell et al. 2007; Beuther et al. 2007). Discriminating between these possibilities is a challenging observational task mostly because high-mass stars form in rich clusters that emit copious amounts of ionising photons that profoundly alter the surrounding environment. This makes it very difficult to ascertain the primordial configuration of the molecular cloud that represents the initial conditions of star formation. Therefore, observational studies of high-mass star-forming regions (SFRs) must consider molecular cores containing young stellar objects (YSOs) that are still in a very early phase of their evolution so that in their impact on the surrounding material should be limited.

One possibility is to identify the earliest stages of high-mass SFRs by means of ammonia ($NH_3$) emission, which traces high-density cores that host newly born O-B type stars. As a first step, we conducted a survey towards 6 SFRs with the Very Large Array (VLA), to detect emission at 1.3 cm of ammonia inversion transitions. The results allowed us to identify 4 sites of high-mass star formation in a phase prior to the appearance of an ultracompact (UC) HII region (Codella et al. 1997, hereafter Paper I). This successful survey has led to extensive follow-up studies at cm- and mm-wavelengths that detected the unique case of G24.78+0.08 A1, an object characaterised by all the "ingredients" of a typical high-mass star formation "recipe": a 20 $M_\odot$ star surrounded by a hypercompact HII region, driving a SiO jet and a CO bipolar outflow, and located at the center of a rotating toroid undergoing infall towards the star (Furuya et al. 2002; Cesaroni et al. 2003; Beltrán et al. 2004, 2005, 2006). These findings support the accretion scenario, but need to be consolidated on statistical grounds by observing more objects of this type.

With this in mind, we extended the pilot VLA survey reported in Paper I to a larger sample of targets. The final goal

of the whole project is to assess how an O-B-type star forms. The main aim of the new observations is twofold: (i) to image and characterise the natal high-density cores that have not yet been destroyed by the high-mass YSOs, and (ii) to identify the youngest and most promising objects at which to apply the same follow-up studies performed for G24.78+0.08.

## 2. Source selection

In order to obtain statistically reliable results, we selected 15 objects from homogeneous VLA surveys towards water masers in high-mass YSOs (Hofner & Churchwell 1996; Forster & Caswell 1989, 2000). Interstellar 22.2 GHz water maser emission represents an excellent tool to search for young protostars, because it is associated with hot molecular cores (HMCs) where the newly formed star is efficiently heating the surrounding medium up to temperatures of hundreds of Kelvin (Cesaroni et al. 1994; Hofner & Churchwell 1996; Kurtz et al. 2000). Several sources of the observed sample are also associated with OH masers at 1.7 GHz (Forster & Caswell 1989), which are usually excited in the material surrounding already formed UC HII regions as well as molecular outflows (e.g., Walsh et al. 2003). Finally, in some sources of the present sample, Class II 6.7 GHz methanol ($CH_3OH$) masers have also been detected (Walsh et al. 1998), which are another excellent tool for the earliest phases of OB-type star formation (e.g., Walsh et al. 2001, 2003).

The $H_2O$ maser positions have an accuracy of $\leq 0\farcs5$. To bias the sample towards the youngest sources, we selected masers that are not associated with developed HII regions. Table 1 lists names, coordinates used as phase centers for the present VLA observations, local standard-of-rest (LSR) velocities, and kinematical distances from the literature. We note that for G31.21–0.18 no distance measurement was found in the literature, whereas for G23.44–0.18, G31.24–0.11, G32.74–0.07, G35.03+0.35, and G48.61+0.02, the distances available in literature were derived using a Galactocentric distance of 10 kpc. For these sources, we derived a revised distance by using the Galactic rotation curve of Brand (1986), which assumes the distance of 8.5 kpc to the Galactic Centre.

**Table 1.** Coordinates used as phase centers for the VLA observations, LSR velocities of the cloud and distances.

| Source | $\alpha$ (J2000) | $\delta$ (J2000) | $V_{LSR}$[a] (km s$^{-1}$) | $d$[b] (kpc) |
|---|---|---|---|---|
| G12.22–0.12 | 18:12:39.81 | –18:24:16.8 | +27.0 | 16.1[c] |
| G12.22–0.12M | 18:12:44.44 | –18:24:24.6 | +28.2 | 16.1[c] |
| G14.17–0.06 | 18:16:26.00 | –16:39:56.2 | +38.3 | 2.5–13.0[d] |
| G23.44–0.18 | 18:34:39.25 | –08:31:38.8 | +99.4 | 5.9[e] |
| G31.24–0.11 | 18:48:45.08 | –01:33:12.8 | +21.8 | 1.7[e] |
| G31.21–0.18 | 18:48:56.57 | –01:36:43.4 | –39.0 | 19.7[e] |
| G31.28+0.06 | 18:48:11.91 | –01:26:38.5 | +108.6 | 8.5[c] |
| G32.74–0.07 | 18:51:21.86 | –00:12:06.2 | +37.5 | 2.7[e] |
| G35.03+0.35 | 18:54:00.65 | +02:01:19.3 | +52.9 | 3.6[e] |
| G35.20–0.74 | 18:58:12.98 | +01:40:38.0 | +33.7 | 2.2[f] |
| G35.20–1.74 | 19:01:45.69 | +01:13:35.0 | +42.6 | 3.3[f] |
| G43.89–0.38 | 19:14:26.17 | +09:22:34.0 | +54.3 | 4.2[g] |
| G48.61+0.02 | 19:20:31.19 | +13:55:24.9 | +19.5 | 9.7[e] |
| G50.32+0.68 | 19:21:27.56 | +15:44:21.3 | +25.8 | 8.7[g] |
| G75.78+0.34 | 20:21:44.11 | +37:26:39.4 | –0.5 | 4.1[g] |

**Notes.** [(a)] Based on the present single-dish survey for all sources but G14.17–0.06 (single-dish CS survey, Plume et al. 1992), G31.21–0.18 (based on the $H_2O$ maser emission pattern, Anglada et al. 1996), G31.24–0.11 (present VLA data), and G50.32+0.68 (single-dish CS survey, Bronfman et al. 1996). [(b)] Whenever the near-far ambiguity is not resolved out both values are reported. [(c)] Walsh et al. (1997). [(d)] Plume et al. (1992). [(e)] Present work. [(f)] Zhang et al. (2009). [(g)] Hofner & Churchwell (1996).

## 3. Observations and data reduction

### 3.1. Single-dish Medicina observations

The Medicina 32-m radiotelescope was used during several runs in October 2002 and May 2004 to observe the $NH_3(1, 1)$ and (2, 2) inversion transitions at 23 694.496 and 23 722.634 MHz, respectively. The half power beam width (HPBW) is $1\farcm9$. The zenith system temperature ranged from 200 K to 800 K depending on weather conditions. The antenna efficiency was 0.38 and the maximum gain 0.11 K Jy$^{-1}$. The intensity scale of the spectra was calibrated on the continuum source DR21, with a resulting uncertainty of 20%. The spectra were corrected for telescope changes with elevation. The pointing accuracy is around $20''$. The observations have been performed in position-switching mode with a 5 min integration time on-source and 5 min off-source. Several scans of each source were obtained for a total integration time between 30 and 140 min. The resulting rms noise is of between 0.05 and 0.15 K in main brightness temperature. The spectra were obtained with a 1024-channel autocorrelator spectrometer, a bandwidth of 8 MHz, and a total velocity coverage of 130 km s$^{-1}$, which produces lines broad enough to cover both $\Delta F = 0, 1$ satellites. The spectral resolution was $\sim$0.11 km s$^{-1}$, smoothed to $\simeq$0.5 km s$^{-1}$ when needed. The conversion factor from main beam brightness temperature to flux density is 5.6 Jy K$^{-1}$.

### 3.2. Interferometric VLA observations

The sources were observed with 26 antennas of the NRAO Very Large Array (VLA) to measure the (2, 2) and (3, 3) (23 722.634 and 23 870.130 MHz, respectively) inversion transitions of ammonia and the 1.3 cm continuum emission. The observations were carried out in the *K*-band with the C-configuration on 2004 February, 22 and 27, and 2004 March, 13 and 18. The HPBW of the antennas is $2\farcm3$, which infers the field-of-view of the images. The largest structure visible in the C-configuration is $\sim 30''$. The phase centers of the 15 sources are listed in Table 1. The $NH_3(2, 2)$ line and the continuum were observed simultaneously by using the correlator in 2 IF mode: (i) a 6.25 MHz bandwidth centered on the line frequency, with a spectral resolution of 97.656 kHz (2.468 km s$^{-1}$); (ii) a 25 MHz bandwidth centered on 23 739.792 MHz to collect continuum emission. For the $NH_3(3, 3)$ line, only one IF was used, centered on the line rest frequency, with a 12.5 MHz bandwidth, and a spectral resolution of 195.313 kHz (9.811 km s$^{-1}$). As for the Medicina observations, the bandwidths were chosen for both lines to be broad enough to cover all the hyperfine components.

The observations were performed in fast-switching mode for a total integration time for each source of about 20 min. Bandpass and phase were calibrated by observing 1733−130, 1851+005, and 1925+211, while the flux density scale was derived by observing 1331+305. All data editing and calibration were carried out using the tasks in the NRAO AIPS package. When both line and continuum were detected, following Paper I, the line cubes were obtained by subtracting the continuum from

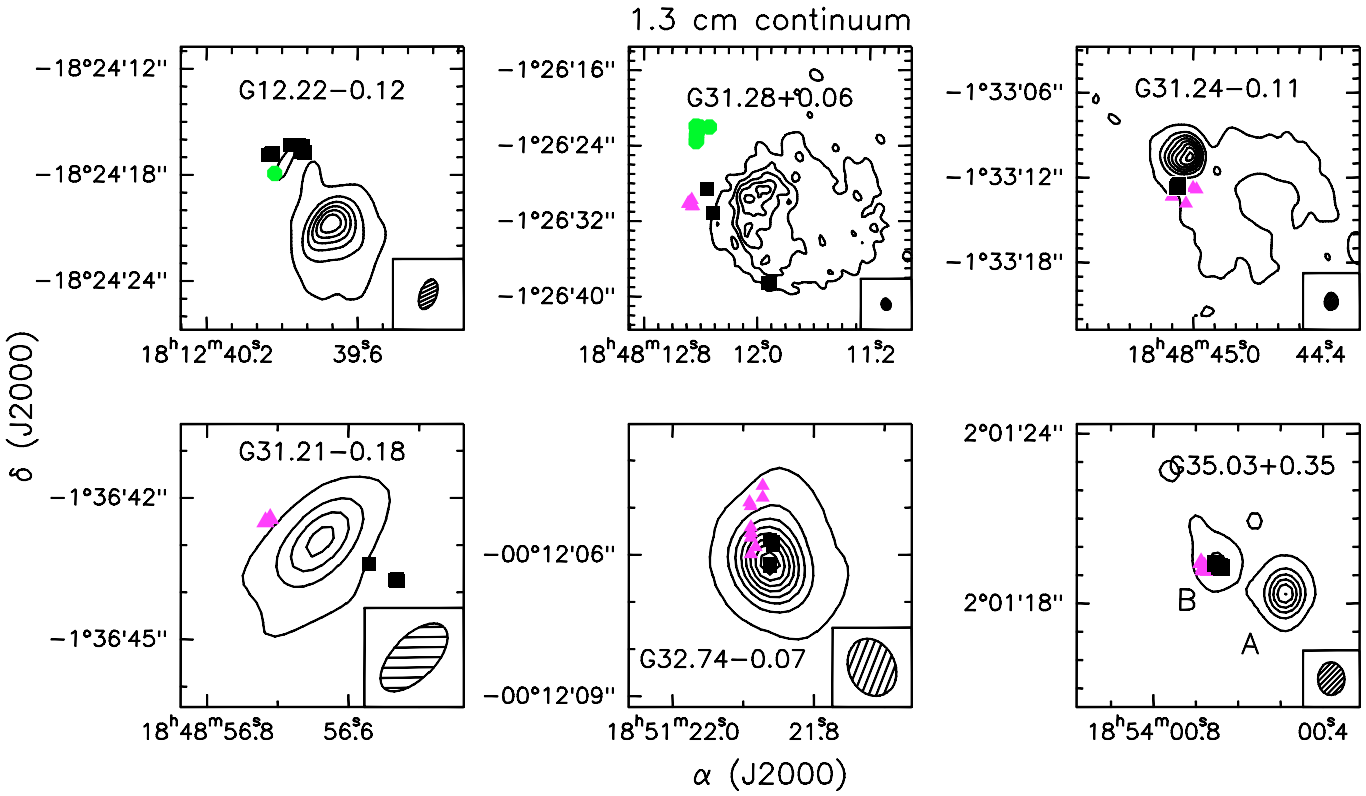


**Fig. 1.** Contour plots of the radio continuum emission in the sources where it has been detected. The squares, green circles, and magenta triangles mark the positions of the $H_2O$, $CH_3OH$, and OH maser spots, respectively (Forster & Caswell 1989; Walsh 1998). The rms $1\sigma$ of the maps is 8 mJy beam$^{-1}$ (G12.22–0.12), 2 mJy beam$^{-1}$ (G31.28+0.06, G31.21–0.18, G32.74–0.07, G35.03+0.35), and 10 mJy beam$^{-1}$ (G31.24–0.11), while the first (negative) contours and the steps correspond to 3 (–3; dotted contour) and $12\sigma$, respectively, for all the sources apart from G31.28+0.06 and G32.74–0.07, where the step corresponds to 6 and $24\sigma$. The ellipses in the bottom-right corners show the HPBW.

the line. Images were produced using natural weighting, and restored with a typical clean beam of $\sim 1''.4 \times 1''$, and a final rms noise of 0.2–1.0 mJy beam$^{-1}$, depending on the source.

## 4. Continuum emission

For 12 out of the 15 sources of the entire sample, we detected continuum emission in the observed field. For two cases (G35.03+0.35, G35.20–1.74) two HII regions were observed (labelled a and b in Fig. 2), whereas for G35.20–0.74, apart from compact emission, two elongated structures, probably associated with a radio-jet oriented in the N-S direction and detected in the mid- and near-IR (Fuller et al. 2001; De Buizer 2006) were detected (labelled jet1 and jet2 in Fig. 2). Details of individual sources are reported in Sect. 5. Figures 1 and 2 report the contour maps, as well as the positions of the $H_2O$, OH (triangles), and $CH_3OH$ (only for G12.22–0.12 and G31.28+0.06, plus G23.44–0.18, not detected in continuum) maser spots, observed by Forster & Caswell (1989) and Walsh et al. (1998). The results confirm the findings of our previous survey (Paper I): the maser spots are observed in the same region, but in most cases they do not coincide positionally with a free-free continuum source, thus tracing a different star-forming site. Three exceptions are G32.74–0.07, G35.03+0.35B, and G35.20–0.74. On the other hand, the $CH_3OH$ maser groups in G31.28+0.06 and G23.44–0.18 do not have any continuum counterpart.

In Table 2, we report the main parameters of the continuum emission in the detected sources: the position of the peak, the flux measured at this position ($F_{peak}$), the corresponding synthesized beam brightness temperature ($T_{SB}$), the observed angular diameter at half power of the emitting region ($\Theta_{HP}$), the beam deconvolved angular diameter ($\Theta_S$), and the integrated flux density over the whole emitting region ($S_\nu$). For the sources spatially unresolved, we arbitrarily assume about one third of the synthesized beam as representing an upper limit to $\Theta_S$. In Table 3, we provide the upper limits to the non-detected sources, corresponding to $3\sigma$ rms values.

In Table 4, the main physical quantities of the related HII regions are given, namely: the physical dimension ($D$); the excitation parameter ($U$); the electron density ($n_e$); the number of Lyman continuum photons emitted by the star per unit time ($N_{Ly}$), computed as in Paper I using the formulae of Schraml & Metzger (1969) and based on the assumption of optically thin emission at 1.3 cm; the luminosity ($L_{bol}$); and the spectral type of the star, derived from $U$ using the tables of Panagia (1973). The properties of the HII regions will be discussed in Sect. 4.2 in the context of the $NH_3$ observations.

### 4.1. Continuum non-detections

We used the upper limits to the continuum emission to constrain the parameters of the (possibly) undetected HII regions, as in Paper I. For a spherical, homogeneous, and isothermal HII region of a given electron temperature ($T_e$), the peak $T_{SB}$ at a given frequency is a function of only the Strömgren radius ($R_S$) and $N_{Ly}$. Thus, for a given distance and frequency it is possible to derive the brightness temperature expected in our synthetised beam $T_{SB}$(calc) as a function of $R_S$ and $N_{Ly}$.

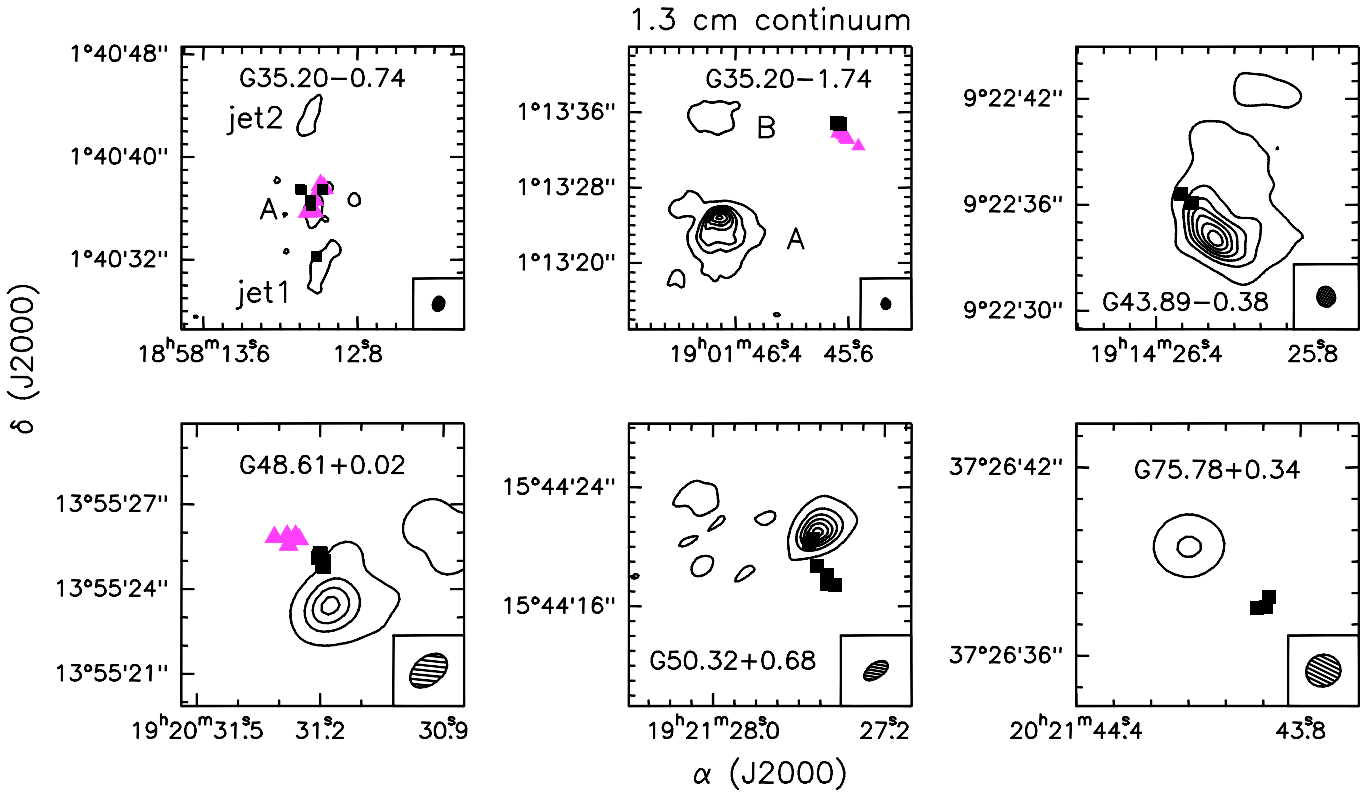


**Fig. 2.** Contour plots of the radio continuum emission in the sources where it has been detected. The squares and magenta triangles mark the positions of the $H_2O$ and OH maser spots, respectively (Forster & Caswell 1989; Walsh 1998). The rms 1$\sigma$ of the maps is 2 mJy beam$^{-1}$ (G35.20–0.74), 3 mJy beam$^{-1}$ (G35.20–1.74), 8 mJy beam$^{-1}$ (G43.89–0.38, G75.78–0.34), 4 mJy beam$^{-1}$ (G48.61+0.02), 5 mJy beam$^{-1}$ (G50.32+0.68), while the first (negative) contours and the steps correspond to 3 (–3; dotted contour) and 12$\sigma$, respectively.

**Table 2.** Parameters of the observed continuum sources shown in Figs. 1 and 2.

| Name | $\alpha$ (J2000) | $\delta$ (J2000) | $F_{peak}$ (mJy beam$^{-1}$) | $T_{SB}$ (K) | $\Theta_{HP}{}^a$ ($''$) | $\Theta_S{}^a$ ($''$) | $S_\nu$ (mJy) |
|---|---|---|---|---|---|---|---|
| HII regions spatially coincident with $H_2O$ masers | | | | | | | |
| G32.74–0.07 | 18:51:21.86 | –00:12:06.2 | 38 | 66 | ~1.0 | ≤0.3 | 42.7 |
| G35.03+0.35B | 18:54:00.65 | +02:01:19.4 | 4 | 8 | ~1.1 | ≤0.4 | 4.4 |
| G35.20–0.74 | 18:58:13.02 | +01:40:36.1 | 2 | 4 | 1.2 | 0.7 | 3.0 |
| HII regions not associated with $H_2O$ masers | | | | | | | |
| G12.22–0.12 | 18:12:39.71 | –18:24:20.7 | 60 | 84 | 5.7 | 5.5 | 210.0 |
| G31.28+0.06 | 18:48:11.93 | –01:26:28.7 | 6 | 11 | 5.8 | 5.7 | 234.0 |
| G31.24–0.11 | 18:48:45.02 | –01:33:10.6 | 92 | 177 | 4.6 | 4.5 | 606.8 |
| G31.21–0.18 | 18:48:56.64 | –01:36:43.0 | 9 | 12 | ~1.0 | ≤0.3 | 9.9 |
| G35.03+0.35A | 18:54:00.49 | +02:01:18.3 | 13 | 26 | ~1.0 | ≤0.3 | 13.6 |
| G35.20–1.74A | 19:01:46.51 | +01:13:24.8 | 234 | 505 | 2.5 | 2.2 | 2351.9 |
| G35.20–1.74B | 19:01:46.62 | +01:13:35.5 | 25 | 53 | 3.6 | 3.5 | 198.3 |
| G43.89–0.38 | 19:14:26.18 | +09:22:34.1 | 67 | 127 | 7.0 | 6.9 | 429.8 |
| G48.61+0.02 | 19:20:31.18 | +13:55:23.4 | 18 | 27 | 1.5 | 0.9 | 29.4 |
| G50.32+0.68 | 19:21:27.52 | +15:44:20.9 | 34 | 42 | 4.2 | 3.9 | 71.5 |
| G75.78+0.34 | 20:21:44.10 | +37:26:39.5 | 2 | 4 | 1.7 | 0.5 | 19.1 |

**Notes.** [a] When the ammonia cores are not spatially resolved, $\Theta_{HP}$ is a measure of the HPBWs of the $NH_3$(2, 2) and (3, 3) maps, whereas we arbitrarily assume about one third of the synthesized beam as an upper limit (used to derive the parameters listed in the table) on $\Theta_S$ (see text).

Figure 3 plots curves of constant $T_{SB}$ corresponding to 3$\sigma$ upper limits (see Table 3): for each source, only points of the $R_S$–$N_{Ly}$ plane falling below the corresponding curve (i.e., satisfying the condition $T_{SB}$(calc) ≤ $T_{SB}$(measured)) are allowed. Each curve can be divided into three sections: (1) at low $R_S$, the size remains constant and corresponds to optically thick and unresolved HII regions; (2) the curve then shows a section where $N_{Ly}$ is constant, corresponding to an unresolved optically thin source; (3) at high $R_S$, we have a resolved and optically thin HII region, with $N_{Ly} \propto {R_S}^2$.

Given the selection criteria, it is reasonable to assume when looking at Fig. 3 that if any UC HII is associated with the maser spots, it may not be detected if it is either too small (<$10^{-4}$–$10^{-3}$ pc) and optically thick or too faint ($N_{Ly}$ < $10^{46}$–$10^{47}$ s$^{-1}$, depending on the source) and optically thin. These two possibilities can be discriminated by estimating the luminosity of the

**Table 3.** Upper limits ($3\sigma$ rms) of the 1.3 cm continuum emission at the $H_2O$ maser position.

| Name | $F_{peak}$ (mJy beam$^{-1}$) | $T_{SB}$ (K) |
|---|---|---|
| G12.22–0.12 | <2.7 | <3.9 |
| G12.22–0.12M | <1.2 | <1.8 |
| G14.17–0.06 | <0.6 | <0.9 |
| G23.44–0.18 | <0.3 | <0.6 |
| G31.28+0.06 | <0.6 | <1.2 |
| G31.24–0.11 | <2.7 | <5.1 |
| G31.21–0.18 | <0.6 | <0.9 |
| G35.20–1.74 | <3.0 | <6.3 |
| G43.89–0.38 | <2.4 | <4.5 |
| G48.61+0.02 | <0.9 | <1.5 |
| G50.32+0.68 | <0.9 | <1.2 |
| G75.78+0.34 | <2.4 | <4.5 |

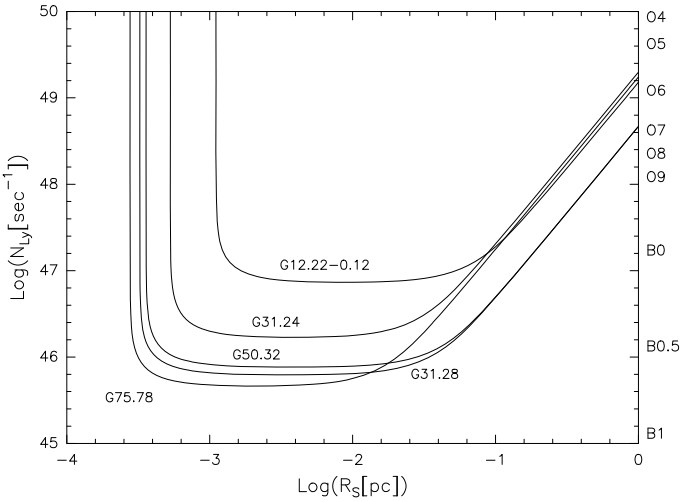


**Fig. 3.** Curves corresponding to constant values of peak brightness temperature in the synthesised beam of a spherical, homogeneous, and isothermal ($T_e$ = 10 000 K) HII region. $R_S$ and $N_{Ly}$ are the Strömgren radius and the Lyman luminosity, respectively. On the right-hand-side axis, the spectral types corresponding to $N_{Ly}$ according to Panagia (1973) are indicated. The contours correspond to the $3\sigma$ upper limits in units of $T_{SB}$ (see Table 3).

region. This can be achieved for a subsample of maser sources (those reported in Fig. 3), which are associated with IRAS point sources. In this way, we obtain high luminosities (between $6 \times 10^4$ and $8 \times 10^5$ $L_\odot$) for all the sources apart from G31.24–0.11 ($5 \times 10^3$ $L_\odot$; spectral type $\simeq$ B1): the corresponding spectral type values suggest the optically thick and spatially unresolved case, supporting the association of $H_2O$ masers with the earliest evolutionary stages of high-mass star formation.

Given the low angular resolution of the IRAS catalogue, we note that the corresponding IRAS bolometric luminosities should be considered as upper limits. As reported in Paper I, it is reasonable to expect values lower by a factor ~5. Nevertheless, although it is clear that only future detections of ionised sources will prove this scenario, this reduction is not enough to invalidate the present suggestion.

## 5. Ammonia emission

### 5.1. Line spectra

We detected $NH_3$(1, 1) and (2, 2) emission in 11 sources (all but G14.17–0.06, G31.21–0.18, G31.24–0.11, and G50.32+0.68) with the single-dish Medicina antenna. The spectra are described in Figs. 4–6. The $3\sigma$ rms upper limits for sources undetected with Medicina are ~60 mK (G31.21–0.18, G31.24–0.11, G50.32+0.68) and 120 mK (G14.17–0.06). Table 5 summarises the observed ammonia spectra parameters: for each line transition we indicate the main beam brightness temperature ($T_{MB}$), the rms noise, the LSR velocity ($V_{LSR}$), and the FWHM linewidth ($\Delta V$) of each hyperfine component. Finally, when the satellite lines are detected, we derive the total optical depth over all the hyperfine components of a transition ($\tau_{tot}$, see Ungerechts et al. 1986).

By using the VLA, we searched for $NH_3$(2, 2) and (3, 3) emission, detecting both lines in 11 of the 15 observed objects: i.e., all apart from G14.17–0.06, G31.21–0.18, G35.20–0.74, and G50.32+0.68. One sees that G35.20–0.74 is detected only in the single-dish spectrum, whereas G31.24–0.11 was detected only with the VLA. The VLA $3\sigma$ rms upper limits for the undetected sources are ~0.6 and 0.3 K for the $NH_3$(2, 2) and (3, 3) lines, respectively. Figures 3–5 show the VLA spectra, obtained by integrating over the whole area where ammonia emission is detected. We note that the Medicina $NH_3$(1, 1) spectra were smoothed to 1 km s$^{-1}$ resolution, whereas the $NH_3$(2, 2) spectra were smoothed to the resolution of the VLA spectra (2.5 km s$^{-1}$) to allow direct comparison.

The main line-intensity ratios of the Medicina to VLA spectra are >1 for all the sources apart from G31.28+0.06, where the ratio is ~1. We note that, besides G12.22–0.12, G23.44–0.18, and G35.20–1.74, the lines observed with the single-dish are more intense by at least an order of magnitude. This suggests that, as found in Paper I, there is an important contribution from an extended emission filtered out by the VLA measurement. In addition, for three sources (G12.22–0.12, G12.22–0.12M, and G35.20–0.74) the ratio of the hyperfine satellites to the main line (indicated by the vertical marks in Figs. 3–5) is higher in the VLA spectra. This finding agrees with the occurrence of a compact optically thick core embedded inside an optically thinner envelope (see also Paper I).

In conclusion, including the 6 sources observed in Paper I, we have detected $NH_3$ in 18 (86%) out of a sample of 21 water maser sites, confirming a close association of $H_2O$ masers with dense ammonia cores. In the next section, we investigate in more detail the distribution of the ammonia emission.

### 5.2. Ammonia cores hosting $H_2O$ masers

Figures 7–10 show the maps of the $NH_3$(2,2) and $NH_3$(3,3) emission integrated beneath the main line. Five sources (G23.44–0.18, G31.24–0.11, G32.74–0.07, G35.03+0.35, and G43.89–0.38) exhibit weak and/or extended emission and do not have a distinctive morphology. This could be caused by more extended (≥40″) emission that is filtered out by the VLA interferometer. On the other hand, 6 regions are associated with 1 or 2 $NH_3$ cores (8 in total), defined here as bright and roundish structures: G12.22–0.12 (A and B), G12.22–0.12 M, G31.28+0.06, G35.20–0.74 (A and B), G48.61+0.02, and G75.78–0.34. Table 6 summarises the ammonia parameters ($T_{MB}$, $V_{LSR}$, $\Delta V$, $\tau_{tot}$) for the sources with extended emission, whereas Table 7 reports those for the 8 $NH_3$ cores. The corresponding $NH_3$(2, 2) and (3, 3) beam-averaged spectra are reported in Fig. 11.

In Figs. 7–10, we mark the positions of the $H_2O$ spots (Forster & Caswell 1989) with black squares. The positions of the OH (triangles) and, in three cases, $CH_3OH$ (G12.22–0.12, G23.44–0.18, and G31.28+0.06; circles) spots are reported

**Table 4.** Derived physical quantities of the HII regions.

| Name | $d$ (kpc) | $D$ (pc) | $U$ (pc cm$^{-2}$) | $n_e$ (cm$^{-3}$) | $N_{Ly}$ ($10^{46}$ s$^{-1}$) | $L_{bol}$ ($L_\odot$) | Spectral Type |
|---|---|---|---|---|---|---|---|
| HII regions spatially coincident with $H_2O$ masers | | | | | | | |
| G32.74–0.07 | 2.7 | ≤0.01 | 10 | $4 \times 10^5$ | 3.1 | $1.3 \times 10^4$ | B0.5 |
| G35.03+0.35B | 3.6 | ≤0.01 | 5 | $2 \times 10^3$ | 0.3 | $6.3 \times 10^3$ | B1 |
| G35.20–0.74 | 2.2 | 0.07 | 2 | $1 \times 10^4$ | 0.02 | $2.0 \times 10^3$ | B2 |
| HII regions not associated with $H_2O$ masers | | | | | | | |
| G12.22–0.12 | 16.1 | 0.43 | 54 | $4 \times 10^3$ | 501.6 | $1.1 \times 10^5$ | O6.5 |
| G31.28+0.06 | 8.5 | 0.23 | 32 | $6 \times 10^3$ | 101.0 | $4.3 \times 10^4$ | O9 |
| G31.24–0.11 | 1.7 | 0.03 | 15 | $2 \times 10^4$ | 10.1 | $1.9 \times 10^4$ | B0 |
| G31.21–0.18 | 19.7 | ≤0.03 | 22 | $1 \times 10^6$ | 35.3 | $2.9 \times 10^4$ | B0 |
| G35.03+0.35A | 3.6 | ≤0.01 | 8 | $17 \times 10^4$ | 1.7 | $1.1 \times 10^4$ | B0.5 |
| G35.20–1.74A | 3.3 | 0.03 | 46 | $1 \times 10^5$ | 301.0 | $7.9 \times 10^4$ | O7.5/O8 |
| G35.20–1.74B | 3.3 | 0.05 | 24 | $2 \times 10^4$ | 42.7 | $3.1 \times 10^4$ | O9.5/B0 |
| G43.89-0.38 | 4.2 | 0.14 | 27 | $8 \times 10^3$ | 63.3 | $3.6 \times 10^4$ | O9.5 |
| G48.61+0.02 | 9.7 | 0.11 | 20 | $3 \times 10^4$ | 51.1 | $2.5 \times 10^4$ | B0 |
| G50.32+0.68 | 8.7 | 0.18 | 25 | $5 \times 10^3$ | 51.1 | $3.4 \times 10^4$ | O9.5 |
| G75.78+0.34 | 4.1 | 0.03 | 10 | $2 \times 10^4$ | 2.9 | $1.3 \times 10^4$ | B0.5 |

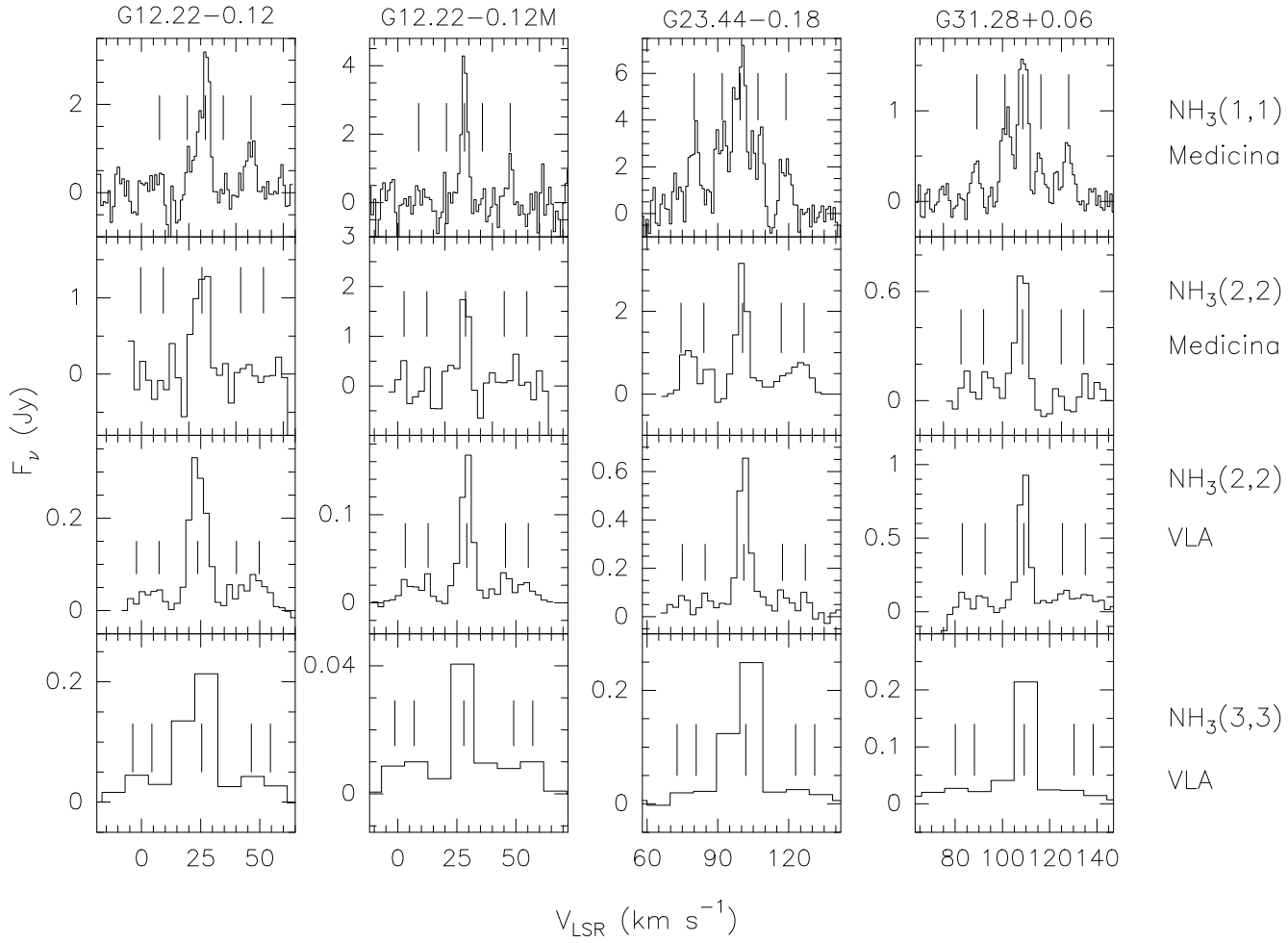


**Fig. 4.** Comparison between the spectra observed with Medicina and VLA. The VLA spectra were derived by averaging the emission over an area covering the whole emitting regions (see text). The vertical lines mark the positions of the hyperfine satellites.

(Walsh 1998; Forster & Caswell 1989). The maps confirm the close association of both the $H_2O$ and OH masers with ammonia emission. We note also from the kinematical point of view that there is good agreement between $H_2O$, OH, and $NH_3$ emission, where the velocities of the maser spots are within 20 km s$^{-1}$. On the other hand, the three $CH_3OH$ maser groups seem to correspond to different sources: they are observed towards both an ammonia clump in G12.22–0.12 and a weak and extended molecular structure in G23.44–0.18, whereas in G31.28+0.06 they are not associated with any ammonia emission. In G12.22–0.12 and G23.44–0.18, there is good agreement between the $CH_3OH$ and $NH_3$ velocities (to within ∼10 km s$^{-1}$).

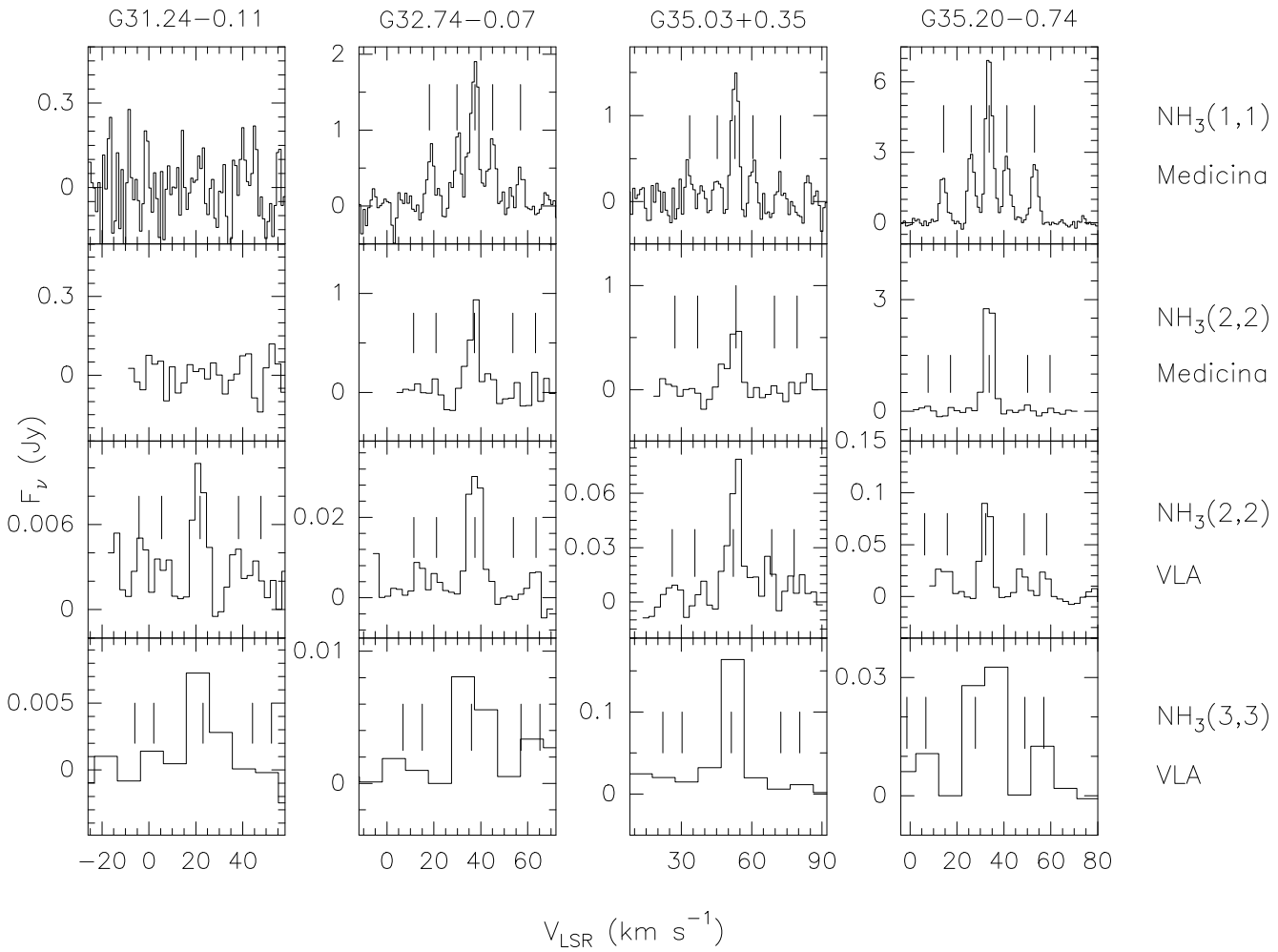


**Fig. 5.** Comparison between the spectra observed with Medicina and VLA. The VLA spectra were derived by averaging the emission over an area covering the whole emitting regions (see text). The vertical lines mark the positions of the hyperfine satellites.

By comparing the ammonia and continuum distributions (see Figs. 1 and 2), we see that all 8 molecular cores apert from G35.20–0.74B show maser emission and no HII region. This result is outlined in the zoom-in of Fig. 12, where the contour plots of the $NH_3$(2, 2) and (3, 3) line satellites, which, being optically thinner with respect to the main line component, are expected to trace the densest part of the ammonia cores. In particular, we plot the G12.22–0.12, G12.22–0.12M, and G35.20–0.74 regions, i.e., those where both the $NH_3$(2, 2) and (3, 3) satellites are clearly detected. The upper panels of Fig. 12 show a superposition of the spatial distribution of the $NH_3$(2, 2) satellites on that of the 1.3 cm continuum, whereas the lower panels compare the maps of the $NH_3$(3, 3) main line with that of the corresponding satellites.

In summary, comparing the 1.3 cm continuum and $NH_3$ maps presented here and in Paper I, we obtain the following results:

1. in 8 (38%) out of 21 cases, no 1.3 cm continuum emission has been detected;
2. in only 4 (19%) cases (the three of the present paper plus G24.78+0.08 A) out of 21, the projected position of the $H_2O$ and OH maser spots coincides with that of the HII regions. The size of these ionised regions is unresolved (≤0.01–0.03), except in the case of G35.20–0.74, whose size is 0.01–0.08 pc. On the other hand, the HII regions present in the observed SFRs but not associated with the maser groups are spatially resolved in all cases apart form G31.21–0.18 and G35.03+0.35A, with larger sizes, of up to 0.43 pc, of on average ∼0.1 pc;
3. in 5 cases (see the G12.22–0.12, G35.20–1.74, G48.61+0.02, G50.32+0.68, and G75.78+0.34 maps), the maser spots are offset from the UCHII regions detected in the same field. The offsets are in the range ∼2″–16″, i.e., of projected distance between ∼0.06 and 0.39 pc. In particular, in the 3 cases where an $NH_3$ core and an UCHII region have been observed in the same SFR (G12.22–0.12, G48.61+0.02, G75.78+0.34), the average distance between the maser spots and the ionised region is up to ∼10 times larger than that between maser spots and ammonia cores.

In the light of these results, we can confirm that $H_2O$ and OH masers trace molecular cores representing the early stages of high-mass star formation, prior to the development of a detectable ionised region or associated with hypercompact HII regions.

### 5.3. Parameters of the ammonia cores

Using the $NH_3$(1, 1) and (2, 2) spectra observed with Medicina and assuming that the ammonia energy levels are populated according to LTE, we estimated the rotation temperature ($T_{rot}$) and

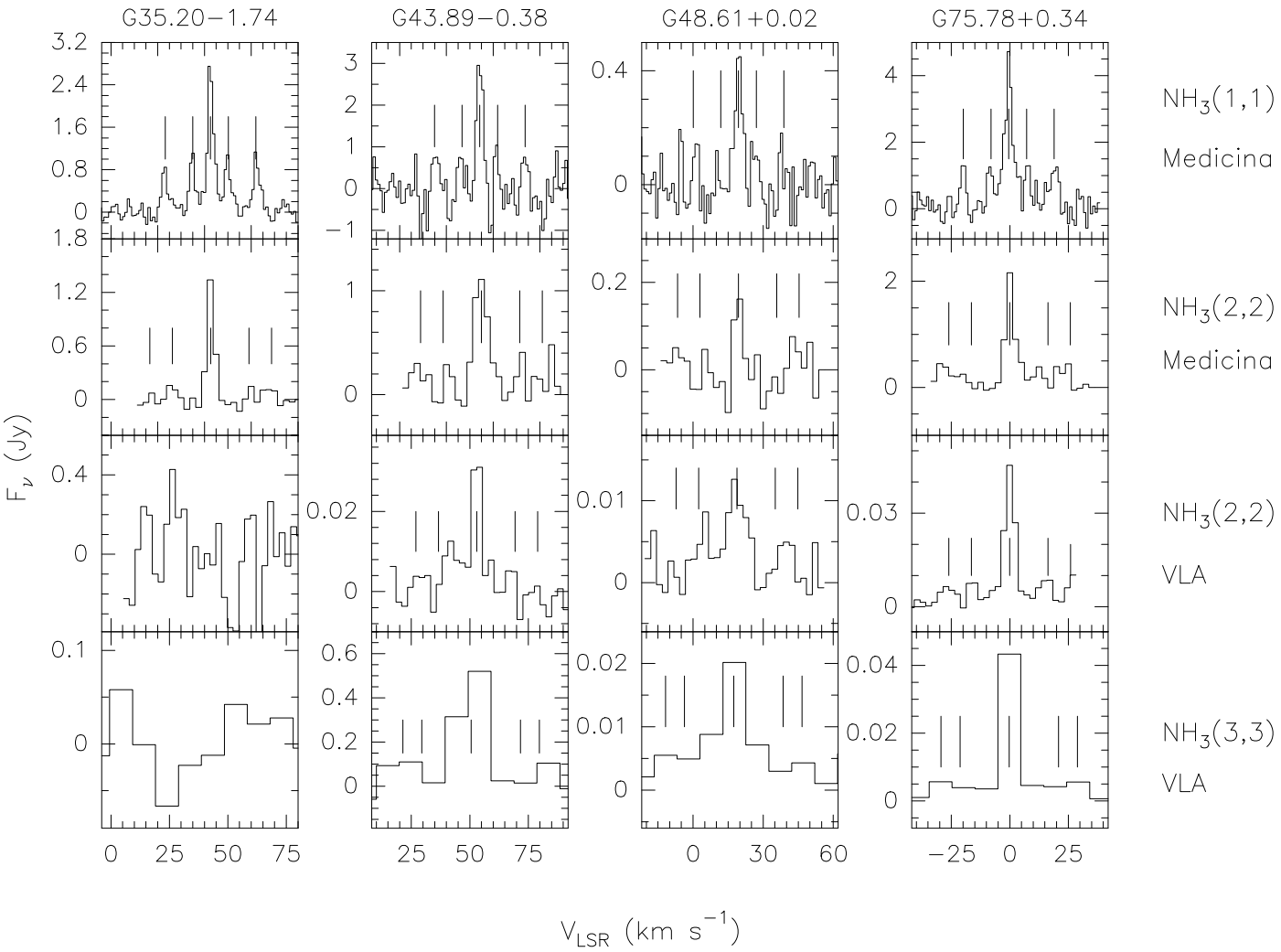


**Fig. 6.** Comparison between the spectra observed with Medicina and VLA. The VLA spectra were derived by averaging the emission over an area covering the whole emitting regions (see text). The vertical lines mark the positions of the hyperfine satellites.

the total column density ($N_{\rm tot}$). The results are summarised in Table 8. We confirm the findings of Paper I, i.e., that the single-dish measurements are sensitive to relatively cold (15–30 K) material. The total ammonia column densities are in the range $10^{13}$–$10^{15}$ cm$^{-2}$. It is very likely that this gas is distributed over more extended regions than those observed with the VLA, as one can argue from the comparison of the line profiles (see Sect. 4.1).

Because of the low spectral resolution used for the $NH_3(3, 3)$ VLA observations (see Sect. 2.2), we cannot derive a reliable optical depth estimate and thus estimate of $T_{\rm rot}$ from the comparison with the $NH_3(2, 2)$ profiles. Thus, we have conservatively assumed a lower limit to the rotation temperature as the maximum brightness temperature measured in the (2, 2) and (3, 3) spectra. As an upper limit we arbitrarily assumed that 100 K is a typical value for HMCs. With this range of temperatures, we calculated the total $NH_3$ column density from that in the (2, 2) level $N_{22}$. This is given in Table 9, where we also list the ammonia beam-averaged column densities of the 8 $NH_3$ cores, obtained from the beam-averaged spectra of Fig. 11. Where no core was detected, we derived the values from the mean spectra by averaging the extended line emission over the $3\sigma$ contours.

In Table 10, we list the physical parameters for the 8 ammonia cores: the observed angular diameter ($\Theta_{\rm HP}$), the beam deconvolved angular ($\Theta_{\rm S}$) and linear diameter ($D$), and the ammonia mass ($M_{\rm NH_3}$), calculated from total column density and size. The diameters of the cores correspond to the full width at half power (FWHP) of the maps of the main ammonia line, averaging the values derived from the $NH_3(2, 2)$ and (3, 3) images.

From the linear diameters of the cores and their $NH_3(2, 2)$ linewidths, one can derive the corresponding virial masses (MacLaren et al. 1998) of $M_{\rm vir}/M_\odot = 0.509\ (d/{\rm kpc})\ (\Theta_{\rm S}/{\rm arcsec})\ (\Delta v/{\rm km\ s^{-1}})^2$. To derive an estimate of the hydrogen density ($n_{\rm H_2}$) and $NH_3$ abundance ($X_{\rm NH_3}$, see Table 10), we assume as we did in Paper I, that the ammonia cores are virialised. Only an estimate of the mass from mm-continuum emission would allow us to verify this assumption. However, for two sources of the Paper I sample (G24.78+0.08 and G24.78+0.08M), we find an agreement of within a factor 2 between the masses derived from the fit to the continuum spectra (Furuya et al. 2002) and the virial masses calculated from the $NH_3$ maps (Codella et al. 1997). We are then confident that the errors caused by our previous assumption are smaller than the typical uncertainties affecting abundance estimates.

When we compare the properties of the 8 ammonia cores detected in the present paper, with those of the 5 cores reported in Paper I, we detect some differences. Our cores are smaller ($\leq$1000–12 000 AU) than those of Paper I (20 000 AU). Since the FWHM of the $NH_3(2, 2)$ lines are almost the same (~6 km s$^{-1}$

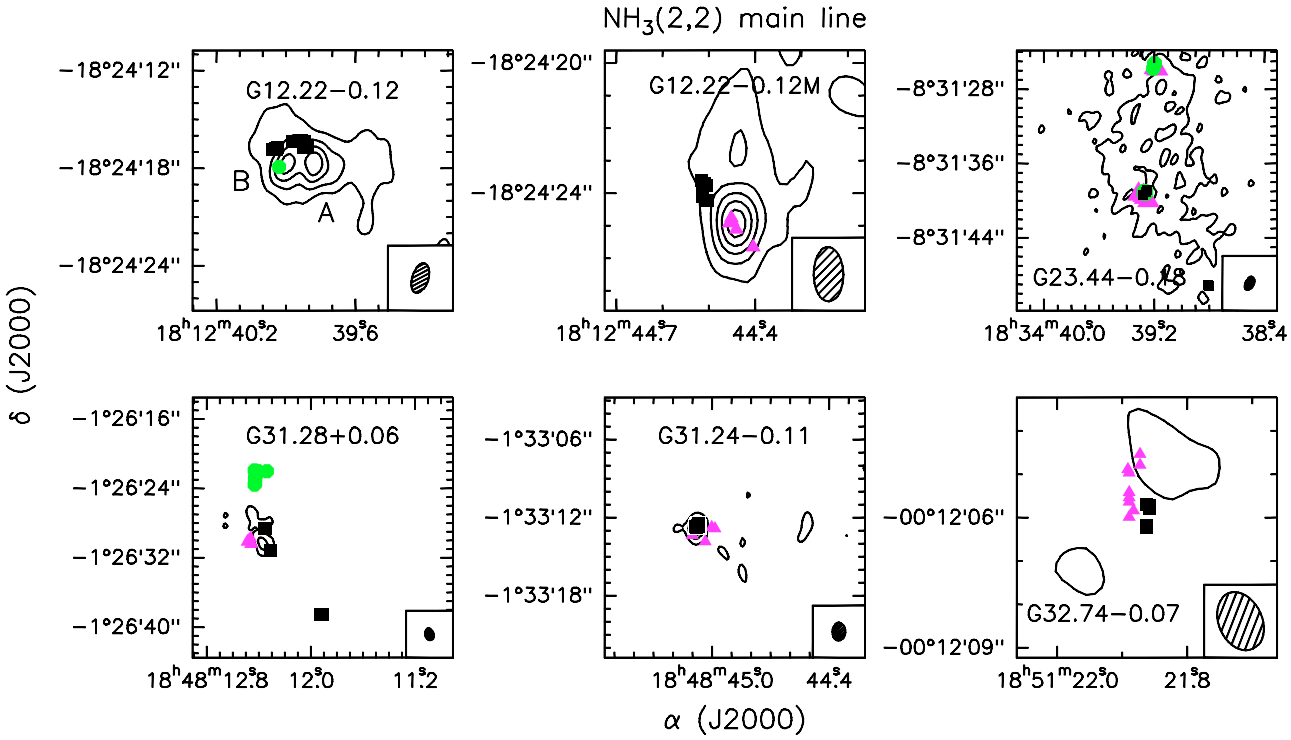


**Fig. 7.** Contour plots of the $NH_3(2, 2)$ line emission integrated under the main line for the sources where it has been detected. When also the continuum emission has been observed, the same region as that of the continuum maps (see Figs. 1 and 2) is shown. The squares, green circles, and magenta triangles mark the positions of the $H_2O$, $CH_3OH$, and OH maser spots, respectively (Forster & Caswell 1989; Walsh 1998). The rms $1\sigma$ of the maps is 1.3 mJy beam$^{-1}$ (G12.22–0.12), 0.8 mJy beam$^{-1}$ (G12.22–0.12M, G31.24–0.11), 0.9 mJy beam$^{-1}$ (G23.44–0.18), and 1.5 mJy beam$^{-1}$ (G31.28+0.06, G32.74–0.07), while both the first (negative) contours and the steps correspond to 3 (–3; dotted contour) $\sigma$. The ellipse in the bottom right corner represents the HPBW.

**Table 5.** Results of fits to the spectra observed at Medicina.

| Name | Line | $T_{MB}$ (K) | rms (mK) | $V_{LSR}$ (km s$^{-1}$) | $\Delta V$ (km s$^{-1}$) | $\tau_{tot}$ |
|---|---|---|---|---|---|---|
| G12.22–0.12[a] | (1,1) | 0.52(0.07) | 81 | +27.0(0.2) | 4.5(0.4) | 0.6 |
| | (2, 2) | 0.26(0.06) | 72 | +25.6(0.4) | 6.7(1.6) | –[b] |
| G12.22–0.12M | (1, 1) | 0.70(0.08) | 127 | +28.2(0.1) | 3.1(0.4) | 0.1 |
| | (2, 2) | 0.36(0.08) | 118 | +28.7(0.3) | 2.8(0.6) | –[b] |
| G23.44–0.18 | (1, 1) | 1.02(0.13) | 153 | +99.4(0.2) | 4.7(0.3) | 4.6 |
| | (2, 2) | 0.53(0.08) | 112 | +100.4(0.2) | 4.0(0.7) | 1.2 |
| G31.28+0.06 | (1, 1) | 0.29(0.03) | 27 | +108.6(0.1) | 4.0(0.2) | 2.7 |
| | (2, 2) | 0.12(0.01) | 22 | +108.5(0.2) | 4.6(0.7) | 0.6 |
| G32.74–0.07 | (1, 1) | 0.31(0.03) | 41 | +37.5(0.1) | 3.4(0.2) | 2.2 |
| | (2, 2) | 0.18(0.03) | 35 | +37.3(0.2) | 3.9(0.9) | –[b] |
| G35.03+0.35 | (1, 1) | 0.26(0.02) | 38 | +52.9(0.1) | 3.2(0.3) | 1.1 |
| | (2, 2) | 0.15(0.02) | 31 | +53.3(0.2) | 2.8(0.6) | –[b] |
| G35.20–0.74[a] | (1, 1) | 1.19(0.04) | 30 | +33.7(0.1) | 3.1(0.1) | 2.3 |
| | (2, 2) | 0.66(0.02) | 26 | +33.7(0.1) | 3.8(0.2) | –[b] |
| G35.20–1.74 | (1, 1) | 0.44(0.03) | 26 | +42.6(0.1) | 2.9(0.2) | 1.7 |
| | (2, 2) | 0.27(0.02) | 26 | +42.7(0.1) | 2.9(0.3) | 1.1 |
| G43.89–0.38 | (1, 1) | 0.56(0.07) | 105 | +54.3(0.1) | 3.0(0.3) | 1.7 |
| | (2, 2) | 0.19(0.04) | 67 | +55.0(0.4) | 5.3(1.0) | –[b] |
| G48.61+0.02 | (1, 1) | 0.08(0.01) | 19 | +19.5(0.2) | 3.7(0.5) | 1.0 |
| | (2, 2) | 0.03(0.01) | 19 | +19.4(0.5) | 3.1(1.1) | –[b] |
| G75.78+0.34 | (1, 1) | 0.69(0.06) | 87 | –0.5(0.1) | 4.1(0.3) | 0.6 |
| | (2, 2) | 0.38(0.05) | 81 | –0.1(0.2) | 3.5(0.7) | –[b] |

**Notes.** [(a)] Given the spatial resolution of the Medicina antenna, the spectra collect the contributions due to both A and B cores (see Figs. 7–10). [(b)] Satellites not detected.

**Table 6.** Extended ammonia emission: results of fits to the spectra derived from the VLA maps.

| Name | line | $T_{MB}$ (K) | rms (mK) | $V_{LSR}$ (km s$^{-1}$) | $\Delta V$ (km s$^{-1}$) | $\tau_{tot}$ |
|---|---|---|---|---|---|---|
| G23.44–0.18 | (2, 2) | 9.0(0.4) | 264 | +101.0(0.1) | 5.0(0.4) | 0.6 |
| | (3, 3) | 5.3(0.1) | 62 | +101.9(0.3) | 10.7(0.5)[a] | 0.7 |
| G31.24–0.11 | (2, 2) | 13.9(2.1) | 1565 | +21.8(0.3) | 4.3(0.5) | –[b] |
| | (3, 3) | 3.7(0.4) | 555 | +23.1(2.4) | 11.5(6.9)[a] | –[b] |
| G32.74–0.07 | (2, 2) | 8.9(0.4) | 195 | +38.1(0.1) | 3.9(0.4) | 0.5 |
| | (3, 3) | 4.0(0.1) | 115 | +38.7(0.5) | 11.1(1.1)[a] | 2.4 |
| G35.03+0.35 | (2, 2) | 5.8(0.6) | 247 | +53.1(0.3) | 5.7(1.3) | –[b] |
| | (3, 3) | 2.5(1.2) | 116 | +51.4(0.8) | 10.3(1.7)[a] | –[b] |
| G43.89–0.38 | (2, 2) | 6.3(0.8) | 684 | +53.0(0.3) | 3.9(1.0) | –[b] |
| | (3, 3) | 1.0(0.1) | 52 | +50.1(3.6) | 9.2(5.1)[a] | –[b] |

**Notes.** [(a)] The larger $\Delta V$ values obtained from the (3, 3) spectra are due to the low spectral resolution (9.8 km s$^{-1}$; see Sect. 2.2). [(b)] Satellites not detected.

here versus ∼5 km s$^{-1}$ in Paper I), this infers smaller virial masses (2–337 $M_\odot$ versus 34–886 $M_\odot$ in Paper I). For the same reason, we also obtain higher densities (1–440 × $10^7$ cm$^{-3}$ versus 7–17 × $10^6$ cm$^{-3}$ in Paper I). On the other hand, the ammonia mass $M_{NH_3}$ is quite low in G35.20–0.74A and B ($10^{-8}$ $M_\odot$) and G75.78+0.34 ($10^{-7}$ $M_\odot$) and is in the range 3 × $10^{-6}$– 1 × $10^{-4}$ $M_\odot$, whereas it has values of between 1 and 70 × $10^{-5}$ $M_\odot$ in Paper I. As a consequence, we infer lower $NH_3$ abundances (0.1–5.1 × $10^{-8}$ versus 0.5–13.9 × $10^{-8}$ in Paper I). The average distances of the ammonia cores of the present sample and of Paper I are similar at ∼8 kpc. In other words, with the present

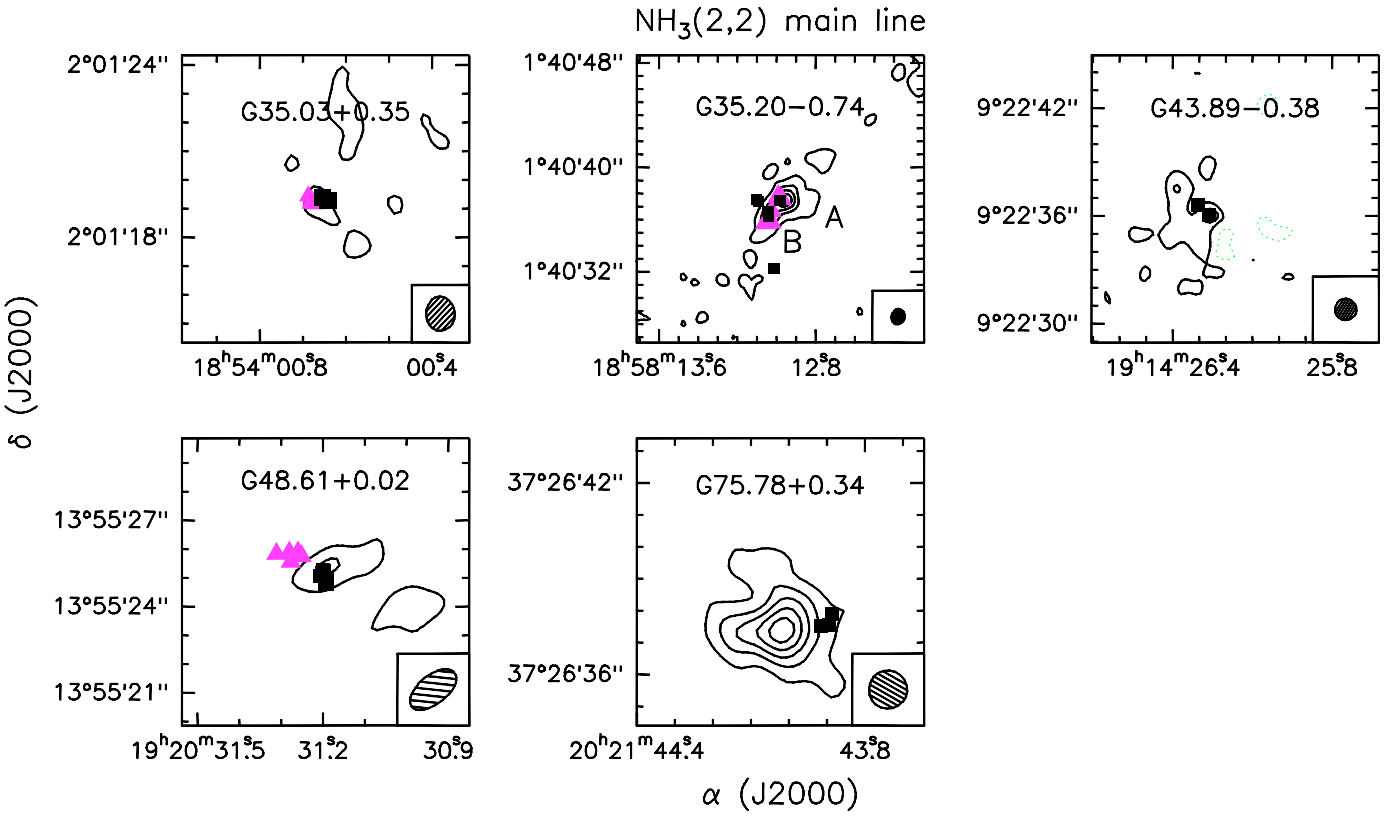


**Fig. 8.** Contour plots of the $NH_3(2, 2)$ line emission integrated under the main line for the sources where it has been detected. When also the continuum emission has been observed, the same region as that of the continuum maps (see Figs. 1 and 2) is shown. The squares and magenta triangles mark the positions of the $H_2O$ and OH maser spots, respectively (Forster & Caswell 1989; Walsh 1998). The rms $1\sigma$ of the maps is 1.2 mJy beam$^{-1}$ (G35.03+0.35, G35.20–0.74), 1.0 mJy beam$^{-1}$ (G43.89–0.38, G48.61+0.02), and 0.9 mJy beam$^{-1}$ (G75.78+0.34), while both the first (negative) contours and the steps correspond to 3 (–3; dotted contour) $\sigma$.

**Table 7.** The ammonia cores: results of fits to the spectra derived from the VLA maps.

| Name | Line | $T_{MB}$ (K) | rms (mK) | $V_{LSR}$ (km s$^{-1}$) | $\Delta V$ (km s$^{-1}$) | $\tau_{tot}$ |
|---|---|---|---|---|---|---|
| G12.22–0.12A | (2, 2) | 28.6(2.9) | 1987 | +24.8(0.3) | 6.8(0.3) | 12.6 |
| | (3, 3) | 46.9(1.4) | 1812 | +24.6(0.4) | 8.4(0.2)[a] | 14.4 |
| G12.22–0.12B | (2, 2) | 35.3(4.3) | 1834 | +21.5(0.3) | 4.2(0.3) | 9.9 |
| | (3, 3) | 33.6(0.9) | 828 | +21.2(0.3) | 9.4(0.4)[a] | 22.2 |
| G12.22–0.12M | (2, 2) | 29.0(2.9) | 869 | +28.6(0.1) | 3.6(0.2) | 13.1 |
| | (3, 3) | 28.3(0.9) | 687 | +27.9(0.2) | 7.7(0.2)[a] | 15.3 |
| G31.28+0.06 | (2, 2) | 24.6(2.2) | 423 | +109.0(0.2) | 4.1(0.3) | 6.0 |
| | (3, 3) | 21.8(0.7) | 223 | +107.9(0.9) | 6.1(1.0)[a] | 6.3 |
| G35.20–0.74A | (2, 2) | 48.7(2.9) | 889 | +32.0(0.1) | 2.4(0.1) | 13.3 |
| | (3, 3) | 17.3(1.4) | 819 | +31.8(0.3) | 6.3(1.0)[a] | 104.0 |
| G35.20–0.74B | (2, 2) | 31.0(3.2) | 881 | +32.0(0.2) | 3.3(0.8) | 2.1 |
| | (3, 3) | 13.6(1.1) | 656 | +28.9(0.7) | 9.5(0.9)[a] | 8.6 |
| G48.61+0.02 | (2, 2) | 6.8(1.5) | 501 | +17.4(1.0) | 11.6(3.8) | 1.2 |
| | (3, 3) | 5.8(0.3) | 223 | +19.0(0.4) | 9.5(0.4)[a] | 25.0 |
| G75.78+0.34 | (2, 2) | 27.9(1.3) | 1113 | +0.6(0.1) | 4.5(0.3) | 2.3 |
| | (3, 3) | 27.9(0.9) | 23 | –0.2(0.3) | 8.9(0.4)[a] | 5.6 |

**Notes.** [(a)] The larger $\Delta V$ values obtained from the (3, 3) spectra are due to the low spectral resolution (9.8 km s$^{-1}$; see Sect. 2.2).

paper we enhance the work of Paper I by observing weaker $NH_3$ cores.

**Table 8.** Ammonia column densities derived from the Medicina spectra.

| Name | $T_{rot}$ (K) | $N_{22}$[a] ($10^{12}$ cm$^{-2}$) | $N_{tot}$[a] ($10^{14}$ cm$^{-2}$) |
|---|---|---|---|
| G12.22–0.12[b] | 26(6) | 22.7(2.3) | 1.5(0.1) |
| G12.22–0.12M | 20(4) | 13.4(4.3) | 1.4(0.1) |
| G23.44–0.18 | 15(2) | 27.5(6.0) | 29.8(2.8) |
| G31.28+0.06 | 17(3) | 7.0(1.3) | 10.8(1.4) |
| G32.74–0.07 | 21(6) | 9.0(2.7) | 6.9(1.2) |
| G35.03+0.35 | 21(3) | 5.4(1.5) | 0.5(0.1) |
| G35.20–0.74[b] | 21(2) | 32.5(1.6) | 9.2(0.6) |
| G35.20–1.74 | 23(2) | 10.1(1.1) | 0.8(0.3) |
| G43.89–0.38 | 23(4) | 13.1(3.8) | 1.1(0.1) |
| G48.61+0.02 | 18(4) | 1.3(0.7) | 0.2(0.1) |
| G75.78+0.34 | 20(3) | 17.4(4.0) | 1.8(0.1) |

**Notes.** [(a)] For all the sources but G23.44–0.18, G31.28+0.06, and G35.20–1.74 (where the optical depths of both ammonia transitions have been derived, see Table 5), we have assumed optically thin emission for the $NH_3(2, 2)$ line. [(b)] Given the spatial resolution of the Medicina antenna, the spectra collect the contributions due to both A and B cores (see Figs. 7–10).

In Fig. 13, we present the distributions of the size and the $NH_3$ relative abundance of the ammonia cores (present paper: 8 cores, Paper I: 5 cores). The distributions of Fig. 13 show that the typical size is $\sim 10^4$ AU, while the typical $NH_3$ relative abundance is $\leq 10^{-7}$, in agreement with the typical

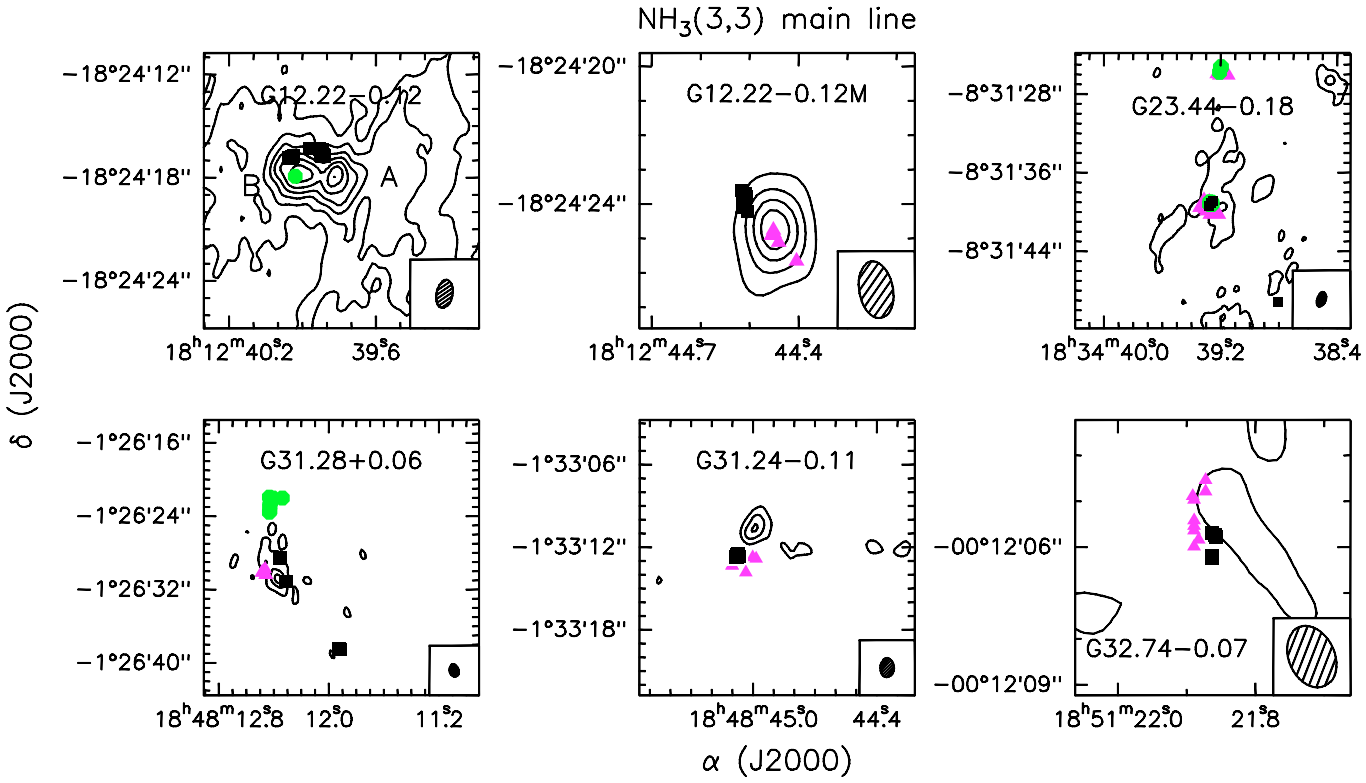


**Fig. 9.** Contour plots of the $NH_3(3, 3)$ line emission integrated under the main line for the sources where it has been detected. When the continuum and/or $NH_3(2, 2)$ emission have also been observed, the same region as that of the continuum and $NH_3(2, 2)$ maps (see Figs. 1 and 2) is shown. The squares, green circles, and magenta triangles mark the positions of the $H_2O$, $CH_3OH$, and OH maser spots, respectively (Forster & Caswell 1989; Walsh 1998). The rms $1\sigma$ of the maps is 1.2 mJy beam$^{-1}$ (G12.22–0.12), 1.5 mJy beam$^{-1}$ (G12.22–0.12M, G31.24–0.11), 0.9 mJy beam$^{-1}$ (G23.44–0.18, G31.28+0.06), and 1.1 mJy beam$^{-1}$ (G32.74–0.07), while both the first (negative) contours and the steps correspond to 3 (–3; dotted contour) $\sigma$. The ellipse in the bottom right corner represents the HPBW.

**Table 9.** Ammonia column densities derived from the VLA maps.

| Name | $T_{rot}$[a] (K) | $N_{22}$[a] ($cm^{-2}$) | $N_{tot}$[a] ($cm^{-2}$) |
|---|---|---|---|
| Extended ammonia emission[b] | | | |
| G23.44–0.18 | ≥9 | $3–30 \times 10^{14}$ | $1–8 \times 10^{16}$ |
| G31.24–0.11 | ≥14 | $0.6–45 \times 10^{14}$ | $0.2–2 \times 10^{16}$[b] |
| G32.74–0.07 | ≥9 | $0.4–45 \times 10^{14}$ | $0.2–12 \times 10^{16}$[b] |
| G35.03+0.35 | ≥6 | $2–30 \times 10^{14}$ | $0.1–18 \times 10^{17}$ |
| G43.89–0.38 | ≥6 | $0.2–41 \times 10^{14}$ | $0.2–230 \times 10^{16}$[b] |
| Ammonia cores | | | |
| G12.22–0.12A | ≥47 | $4–9 \times 10^{16}$ | $2–4 \times 10^{17}$ |
| G12.22–0.12B | ≥36 | $2–4 \times 10^{16}$ | $7–17 \times 10^{16}$ |
| G12.22–0.12M | ≥29 | $1–5 \times 10^{16}$ | $8–12 \times 10^{16}$ |
| G31.28+0.06 | ≥25 | $6–26 \times 10^{15}$ | $4–10 \times 10^{16}$ |
| G35.20–0.74A | ≥49 | $2–3 \times 10^{16}$ | $6–12 \times 10^{16}$ |
| G35.20–0.74B | ≥31 | $2–7 \times 10^{15}$ | $1–3 \times 10^{16}$ |
| G48.61+0.02 | ≥7 | $1–14 \times 10^{15}$ | $5–210 \times 10^{16}$ |
| G75.78+0.34 | ≥28 | $3–9 \times 10^{15}$ | $2–4 \times 10^{16}$ |

**Notes.** [(a)] Given the low spectral resolution (see Sect. 2.2) of the $NH_3(3, 3)$ spectra, we estimated a lower limit for $T_{rot}$ as the maximum $T_{MB}$ value shown by the (2, 2) and (3, 3) spectra. As an upper limit we arbitrarily assumed 100 K. [(b)] The column densities derived for G31.24–0.11, G32.74–0.07, and G43.89–0.38 are very approximative due to no optical depth measurement (see Table 5): in this case $\tau_{tot}$ = 0.1–1 has been arbitrarily assumed.

values observed for Orion ($10^{-8}$–$10^{-7}$; van Dishoeck & Blake 1998).

## 6. Comments on individual sources

### 6.1. G12.22–0.12

Although ammonia has already been observed towards this region (Cesaroni et al. 1992; Anglada et al. 1996), until now no maps have been obtained for any $NH_3$ transition. In Fig. 12, two ammonia peaks devoid of 1.3 cm continuum emission are seen, which are offset from the continuum peak. Given the proximity of the $H_2O$ masers to the ammonia cores, it is likely that the three sources within the map field (the two ammonia cores and the UC HII region) are associated with high-mass YSOs.

The position and distribution of the 1.3 cm continuum emission are consistent with those obtained at 3 cm with the Australia Telescope Compact Array (ATCA) by Forster & Caswell (2000), who describe it as a cometary UC HII region. The same authors suggest that this source might be located at a distance smaller than 16.1 kpc, because of the extent of the UC HII region and the $H_2O$ maser spots. The flux density, $S_\nu$, was measured towards the UC HII region at 9 GHz by Forster & Caswell (2000) and at 1.4 and 5 GHz by Becker et al. (1994): the index of the spectral energy distribution between 23 and 9 or 5 GHz is ~0.2–0.3, indicating that at 23 GHz the free-free emission is optically thin.

G12.22–0.12 was detected in different molecular tracers that, beside $NH_3$, include CS (Plume et al. 1992) and $CH_3CN$ (Olmi et al. 1993), thus making it a reliable hot molecular core (HMC) candidate. It is reasonable to conclude that the $CH_3CN$ line emission mostly originates in the $NH_3$ cores of Fig. 12. This region was also mapped at 450 and 850 $\mu$m by Hatchell et al. (2000) and

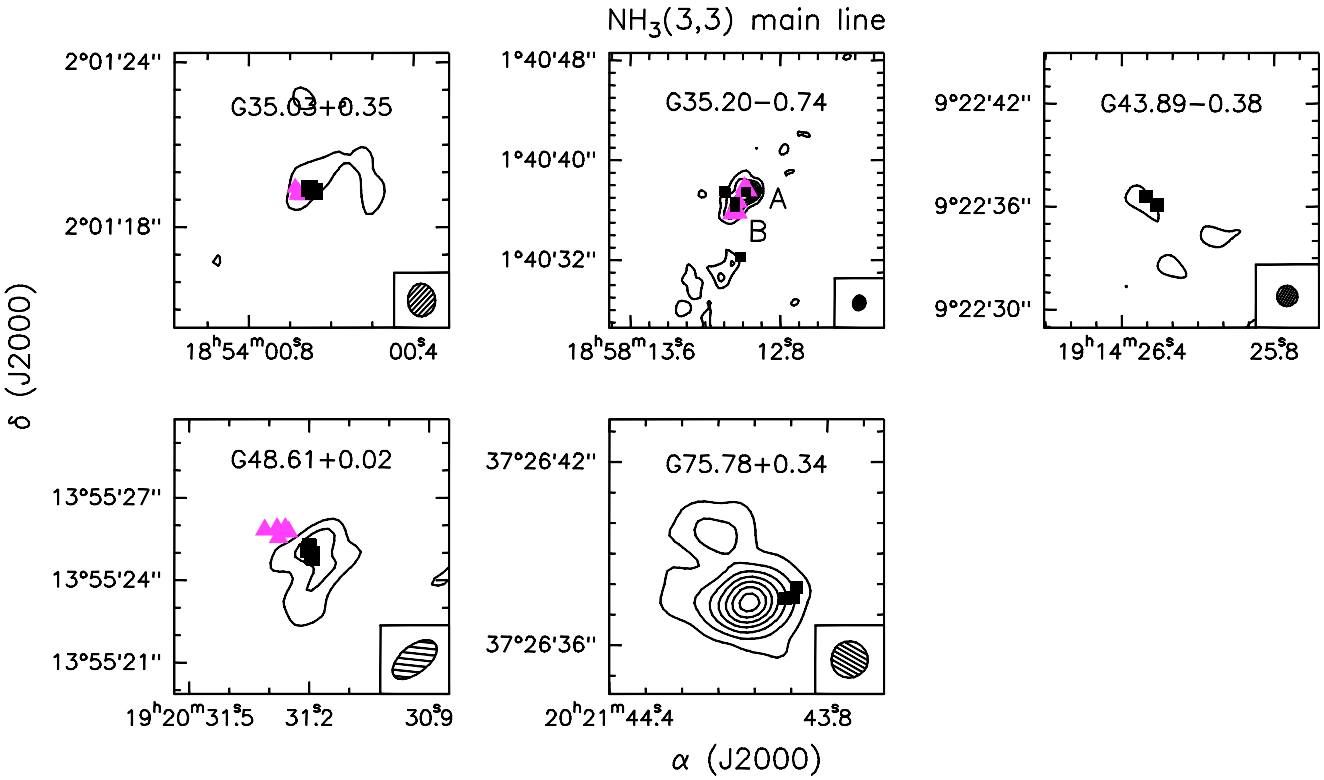


**Fig. 10.** Contour plots of the $NH_3(3, 3)$ line emission integrated under the main line for the sources where it has been detected. When the continuum and/or $NH_3(2, 2)$ emission have also been observed, the same region as that of the continuum and $NH_3(2, 2)$ maps (see Figs. 1 and 2) is shown. The squares and magenta triangles mark the positions of the $H_2O$ and OH maser spots, respectively (Forster & Caswell 1989; Walsh 1998). The rms $1\sigma$ of the maps is 1.3 mJy beam$^{-1}$ (G35.03+0.35) 0.5 mJy beam$^{-1}$ (G35.20–0.74), 2.6 mJy beam$^{-1}$ (G43.89–0.38), 0.7 mJy beam$^{-1}$ (G48.61+0.02), 0.9 mJy beam$^{-1}$ (G75.78+0.34), while both the first (negative) contours and the steps correspond to 3 (–3; dotted contour) $\sigma$.

**Table 10.** Parameters of the ammonia cores derived from the VLA maps.

| Name | $\Theta_{HP}{}^a$ ($''$) | $\Theta_S{}^a$ ($''$) | $D$ ($10^3$ AU) | $M_{NH_3}{}^a$ ($10^{-6}$ $M_\odot$) | $M_{vir}{}^a$ ($M_\odot$) | $n_{H_2}{}^a$ ($10^9$ cm$^{-3}$) | $X_{NH_3}{}^a$ ($10^{-9}$) |
|---|---|---|---|---|---|---|---|
| G12.22–0.12A | 1.6 | 0.8 | 12.1 | 120.8 | 303 | 0.10 | 46 |
| G12.22–0.12B | 1.6 | 0.8 | 12.1 | 48.3 | 187 | 0.06 | 30 |
| G12.22–0.12M | ~1.5 | ≤0.5 | ≤8.1 | 15.6 | 53 | 0.07 | 35 |
| G31.28+0.06 | 1.3 | 0.5 | 4.0 | 2.9 | 36 | 0.34 | 9 |
| G35.20–0.74A | ~1.2 | ≤0.3 | ≤0.6 | 0.05 | 2 | 0.01 | 3 |
| G35.20–0.74B | ~1.2 | ≤0.3 | ≤0.6 | 0.01 | 4 | 0.03 | ~1 |
| G48.61+0.02 | 1.4 | 0.5 | 8.2 | 147.3 | 337 | 2.20 | 51 |
| G75.78+0.34 | ~1.3 | ≤0.3 | ≤1.2 | 0.1 | 13 | 4.40 | 1 |

**Notes.** [(a)] When the ammonia cores are not spatially resolved, $\Theta_{HP}$ is equal to the HPBWs of the $NH_3(2, 2)$ and (3, 3) maps, whereas we arbitrarily assume that HPBW/3 is an upper limit (used to derive the parameters listed in the table) of $\Theta_S$ (see text).

at 350 $\mu$m by Hunter et al. (2000). In all three cases, the emission comes from the whole area mapped in Fig. 12 and the angular resolution is too low to safely associate the peak of the emission with any of the three sources resolved by our observations.

### 6.2. G12.22–0.12M

This source was detected and mapped at several submillimeter wavelengths by Hatchell et al. (2000; 450 and 850 $\mu$m) and Hunter et al. (2000; 350 $\mu$m). Although associated with $H_2O$ and OH masers, and with $NH_3$ emission (Anglada et al. 1996; see also Fig. 12), it shows detectable continuum emission at neither 3 cm (Forster & Caswell 2000) nor 1.3 cm (this work). All of these findings suggest that this source hosts one or more high-mass YSOs deeply embedded in a dense molecular core where no detectable HII region has yet been formed.

### 6.3. G35.20–0.74

Previous radio continuum observations carried out by Dent et al. (1984; 5 GHz) and Gibb et al. (2003; 5 and 8.5 GHz) with the VLA detected a north-to-south radio jet in this region, which is also detected in the mid- and near-IR by De Buizer (2006) and Fuller et al. (2001), respectively. The maps obtained by Gibb et al. (2003) show evidence that the jet is precessing. This can be seen from the S-shaped distribution of most of the radio sources detected by the cited authors (denoted by circles in Fig. 14). The present 1.3 cm continuum observations confirm the presence of a radio jet oriented along the N-S direction (Fig. 2), and

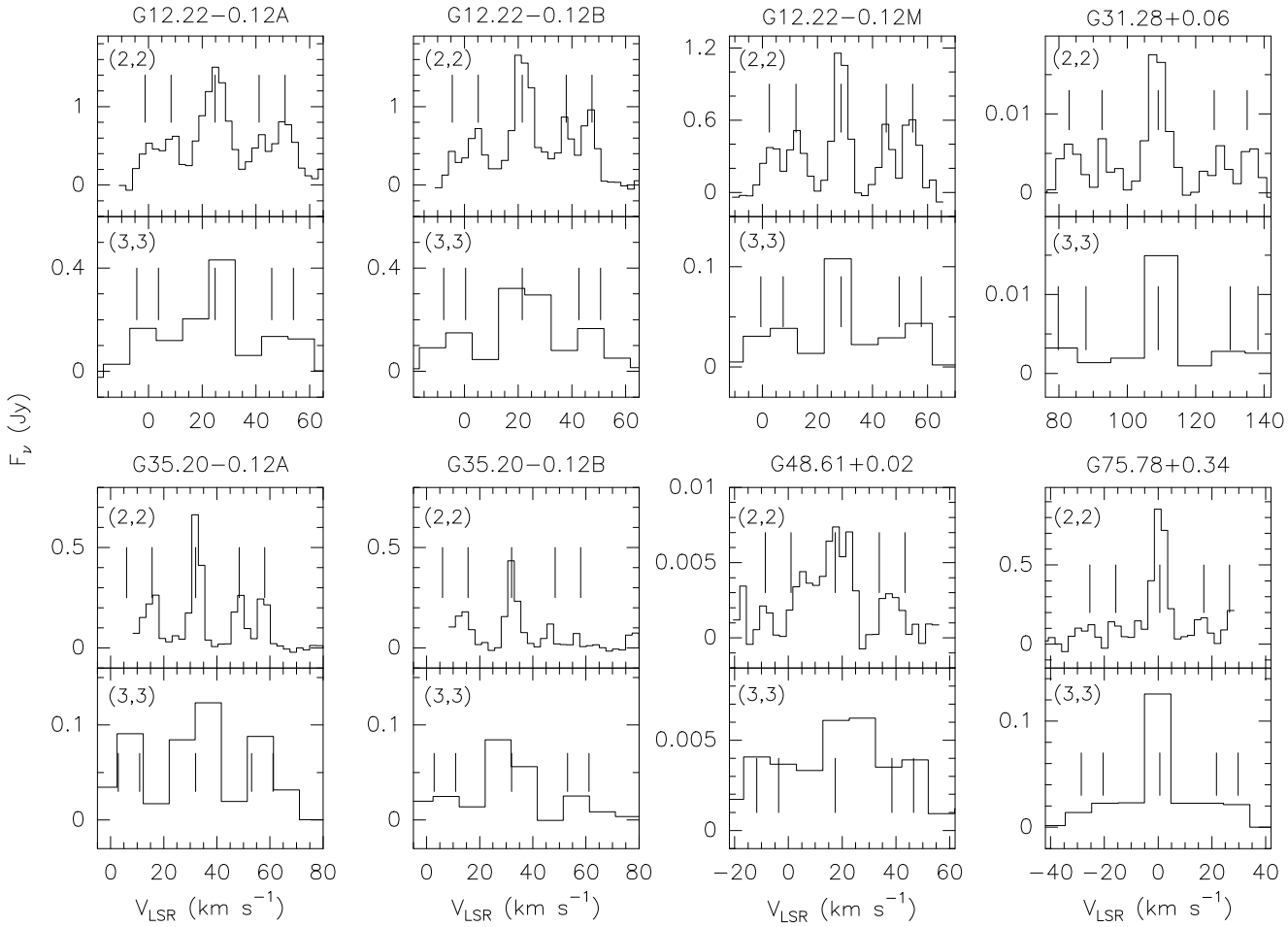


**Fig. 11.** Ammonia (2, 2) and (3, 3) VLA beam averaged spectra of the 8 $NH_3$ cores (see text) shown in Figs. 7–10. The vertical lines mark the positions of the hyperfine satellites. Due to technical problems, part of the $NH_3$(2, 2) spectra of G35.20–0.74 and G75.78–0.34 is missing.

the shapes and orientations of the southern and northern components (labeled jets 1 and 2, respectively) are also consistent with precession, in agreement with the results reported by Gibb et al. (2003).

A close-up view of the central part of this region reveals two $NH_3$ cores, called A and B in Fig. 12. Source A is clearly detected in both $NH_3$(2, 2) and (3, 3), but has no detectable 1.3 cm continuum emission. In contrast, source B displays 1.3 cm continuum emission and weak ammonia emission. The coordinates of source B coincide with those of the UC HII region known as G35.20N (also named Source 7 by Gibb et al. 2003). According to these authors this source drives the precessing radio-jet. Source A does not have a radio continuum counterpart at either 5 or 8.5 GHz, (see Fig. 6 of Gibb et al. 2003). However, it appears to be centered on the peak of the $H^{13}CN(1-0)$ emission presented by the same authors. Added to the presence of $H_2O$ and OH masers, this suggests that source A contains one or more high-mass YSOs and is more deeply embedded and possibly less evolved than source B.

A molecular outflow oriented in the SW-NE direction was observed by Gibb et al. (2003) and López-Sepulcre et al. (2009; Fig. 14) in $^{12}CO$ and $^{13}CO$, respectively. On the basis of these different jet/outflow orientations, Gibb et al. (2003) argue that this region contains multiple outflows, instead of the precessing flow proposed by Little et al. (1998). They also suggest that the CO outflow is driven by the millimeter source G35MM2 (marked with an asterisk in Fig. 14). However, by examining Fig. 14, it seems more plausible that the center of the flow is either source A or B, and thus the idea of precession should not be excluded, even if it implies a precession angle of 58°. Assuming the velocity of the jet to be ~100 km s$^{-1}$, we derive a kinematical age of ~10 000 yr, and hence the angular velocity of the precession comes to ~20″ yr$^{-1}$. This value is similar to that found for IRAS 20126+4104 (~60″ yr$^{-1}$) by Cesaroni et al. (2005), making the interpretation of precession plausible. Higher angular resolution observations in a suitable molecular outflow tracer would help us to identify the driver and discriminate between precession and outflow multiplicity.

Finally, $C^{18}O(2-1)$ velocity maps obtained by López-Sepulcre et al. (2009) show a NW-SE velocity gradient of ~1.3 km s$^{-1}$ over 0.3 pc, perpendicular to the $^{13}CO$ outflow axis. Although sources A and B are aligned along the direction of this gradient, they both have the same $V_{LSR}$ velocities, as seen from Table 7, i.e., ~+32.0 for both A and B. Therefore, the present $NH_3$ maps imply that the observed velocity gradient is not caused by sources A and B having different systemic velocities, and the interpretation of a flattened structure rotating perpendicularly to the outflow axis remains plausible.

### 6.4. G75.78+0.34

Towards G75.78+0.34 evidence of compact and high-temperature gas (~85 K) has been found using single-dish observations of hot-core tracers such as $CH_3CN$ and $NH_3$(4, 4)

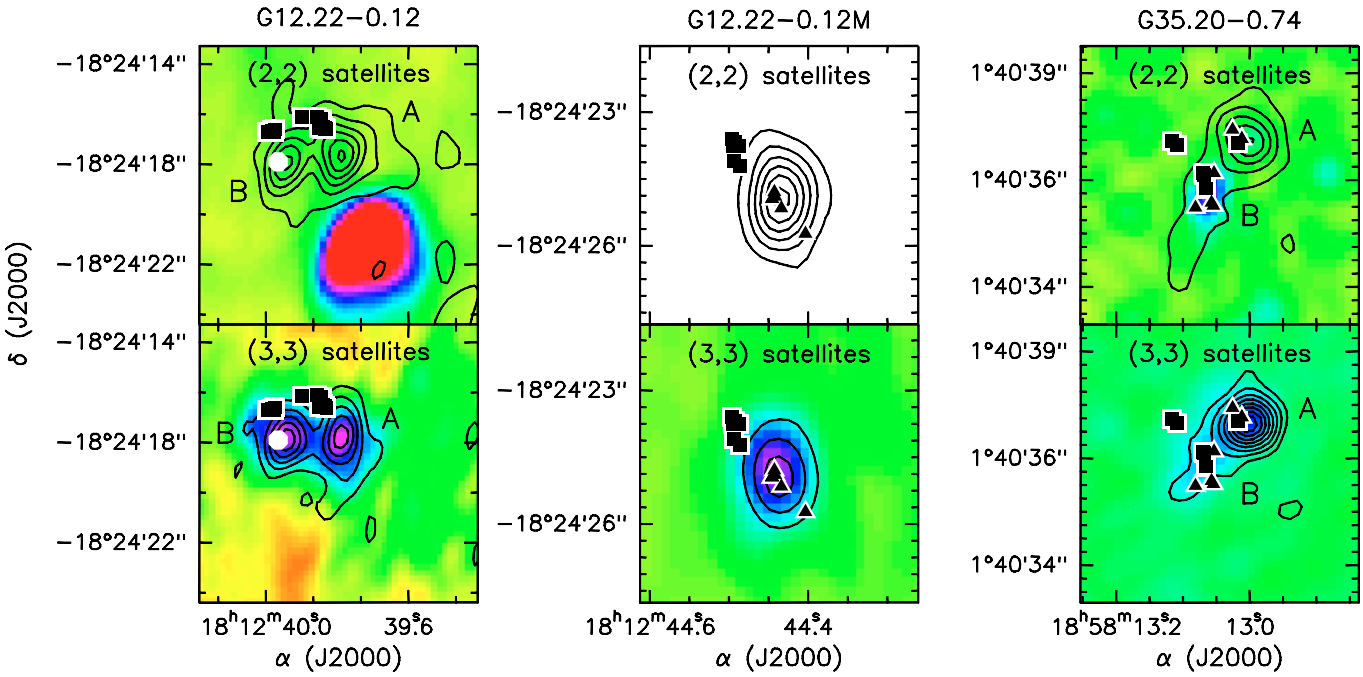


**Fig. 12.** *Upper panels*: contour plots of the $NH_3(2, 2)$ line intensity integrated under the satellites for G12.22–0.12 (*left*), G12.22–0.12M (*middle*), and G35.20–0.74 (*right*). The rms $1\sigma$ of the maps is 0.6 (G12.22–0.12), 0.5 (G12.22–0.12M), and 0.4 mJy beam$^{-1}$ (G35.20–0.74). Both the first contours and the steps correspond to $3\sigma$. The colour scale represents the 1.3 cm continuum (see Figs. 1 and 2). The squares, circles, and triangles mark the positions of the $H_2O$, $CH_3OH$, and OH maser spots, respectively (Forster & Caswell 1989; Walsh 1998). *Lower panels*: contour plots of the $NH_3(3, 3)$ intensity integrated by the satellites. The rms $1\sigma$ of the maps is 0.6 (G12.22–0.12), 0.5 (G12.22–0.12M), and 0.4 mJy beam$^{-1}$ (G35.20+0.74). Both the first (negative) contours and the steps correspond to 3 (–3; dotted contour) $\sigma$. The colour scale represents the integrated $NH_3(3, 3)$ main line intensity (see Figs. 9 and 10).

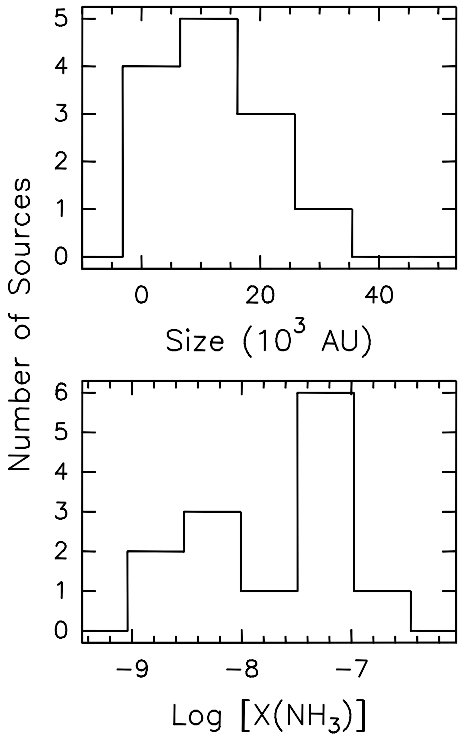


**Fig. 13.** Distributions of the size of the $NH_3$ cores (*upper panel*) and their relative $NH_3$ abundance with respect to $H_2$ (*lower panel*). The values correspond to the 13 cores (present paper: 8, Paper I: 5).

and (5, 5) by Olmi et al. (1993). The present $NH_3$ maps indicate that, as described for the three regions previously discussed, two different sources are seen in G75.78+0.34: one with 1.3 cm continuum emission and only weak ammonia emission, and a second one detected in the ammonia lines but not in the 1.3 cm continuum, located about 2″ south of the radio continuum source (Figs. 2, 8, and 10).

Evidence of molecular outflows has been found in this region. Shepherd et al. (1997) carried out high-angular resolution $^{12}$CO and SiO observations with the Berkeley-Illinois-Maryland Array (BIMA), detecting a total of four outflows. On the basis of their location, two of these (referred to as Central and Western by the same authors) could be associated with one or both sources detected in the present work, although the resolution of their images is not high enough to permit a clear identification. Further evidence of outflowing motions was reported by López-Sepulcre et al. (2009), who imaged the region in the $^{13}$CO(2–1) line with the IRAM 30-m telescope. The resulting blue and red lobe maps are represented as contours in Fig. 15, superimposed on the 1.3 continuum map (upper panel) and $NH_3(2, 2)$ main line-emission map (lower panel). Even though the outflow lobes are not very clearly defined, the disposition of the blue-shifted emission suggests an association with the radio continuum source. However, only sufficiently high-spatial resolution images can confirm this, and whether the YSOs hidden in the $NH_3$ core are also powering an outflow.

## 7. Summary and conclusions

We have investigated 15 high-mass SFRs in the $NH_3(1, 1)$, (2, 2), and (3, 3) lines as well as in the 1.3 cm continuum emission with the single-dish Medicina antenna and the VLA interferometer. The sample has been selected from surveys of $H_2O$ and OH masers, to target earliest phases of high-mass star formation. The

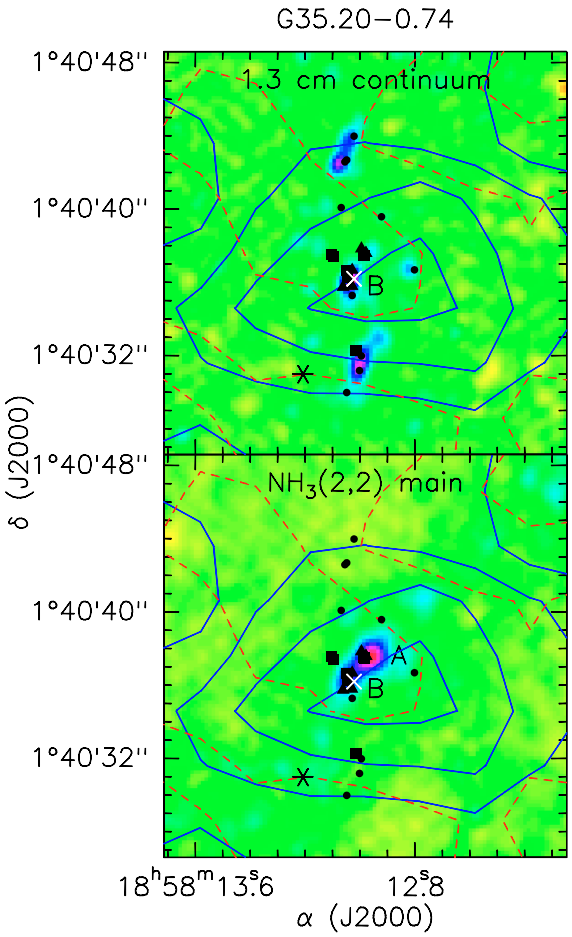


**Fig. 14.** *Upper panel*: contour plots of the $^{13}$CO(2–1) blue (solid) and red (dashed) line wing emission (from López-Sepulcre et al. 2009), superimposed on the VLA 1.3 cm continuum map (colour scale) of G35.20−0.74. *Lower panel*: contour plots of the $^{13}$CO(2–1) blue (solid) and red (dashed) line wing emission superimposed on the $NH_3$(2, 2) emission integrated beneath the main line (colour scale). Contours start from 5$\sigma$ and increase in steps of 5$\sigma$, with 1$\sigma$ = 0.2 K for both the blue and red lobe emission. The squares and triangles mark the positions of the $H_2O$ and OH maser spots, respectively (Forster & Caswell 1989; Walsh et al. 1998). The white cross and the asterisk correspond to the radio source G35.2N (Source B) and the millimeter source G35MM2, respectively (coordinates taken from Gibb et al. 2003). Circles represent the radio sources detected by Gibb et al. (2003) at 5 and 8.5 GHz.

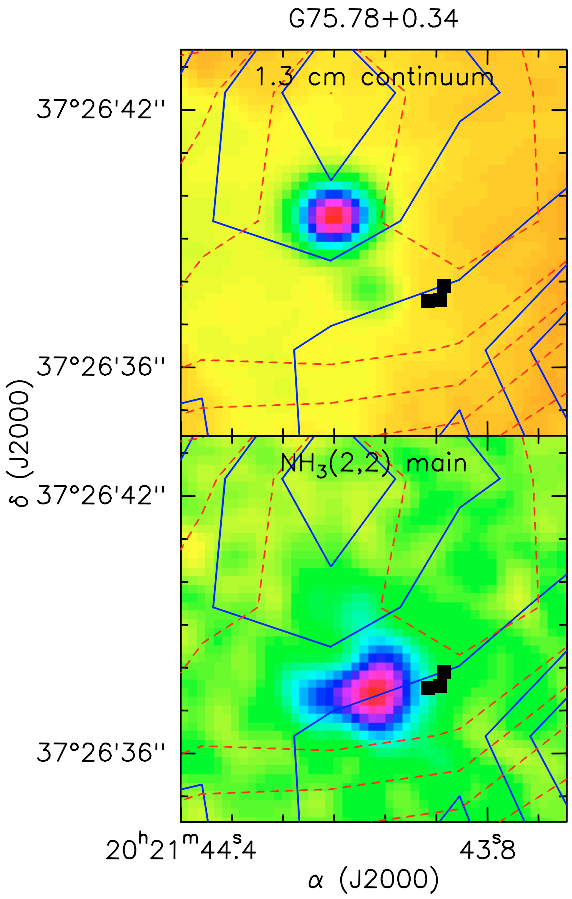


**Fig. 15.** *Upper panels*: contour plots of the $^{13}$CO(2–1) blue (solid) and red (dashed) line wing emission (from López-Sepulcre et al. 2009), superimposed on the VLA 1.3 cm continuum map (colour scale) of G75.78+0.34. *Lower panel*: contour plots of the $^{13}$CO(2–1) blue (solid) and red (dashed) line wing emission superimposed on the $NH_3$(2, 2) emission integrated under the main line (colour scale). Contours start at 5$\sigma$ and increase by steps of 1$\sigma$, with 1$\sigma$ = 0.4 K for the blue lobe emission and 0.5 K for the red lobe emission. The squares and triangles mark the positions of the $H_2O$ and OH maser spots, respectively (Forster & Caswell 1989).

present project completes the pilot survey started in Paper I with the aim of characterising the natal high-density molecular cores not yet destroyed by the newly formed high-mass YSOs.

The main results are the following:

1. We have detected continuum emission in almost all the observed star-forming regions that traces extended and UCHII regions created by YSOs with typical luminosities of $\sim 10^4$ $L_\odot$. In only 3 cases do we observe a positional coincidence between UCHII regions and $H_2O$ and OH maser spots. The upper limits to the continuum emission towards the rest of the maser spots can be used to constrain the parameters of the undetected HII regions. We suggest that the lack of detection is caused by optically thick and spatially unresolved sources.
2. Ammonia emission has been detected towards 12 SFRs with Medicina and/or VLA. By comparing between the Medicina and VLA spectra, we identify an extended envelope resolved by the interferometer. The VLA ammonia images detect weak extended emission without a clear morphology in 5 SFRs, whereas 6 regions are clearly related to 1 or 2 $NH_3$ cores (8 in total) closely associated with the $H_2O$ and OH maser spots.
3. The statistical analysis of the distribution between $H_2O$ and OH masers, $NH_3$ cores, and HII regions allows us to confirm that the molecular cores trace the early stages of high-mass star formation, prior to the development of a detectable ionised region or, at most, associated with hypercompact HII regions (≤0.01 pc).
4. The ammonia cores have a typical size of $\sim 10^4$ AU and high masses (up to $10^4$ $M_\odot$), and are very dense (up to fews $10^9$ cm$^{-3}$). The temperatures are estimated to be on average greater than ∼30 K. Most of the molecular cores have a relative $NH_3$ abundance of $\leq 10^{-7}$, in agreement with the values observed in the Orion region.

*Acknowledgements.* A.L.S. aknowledges support from the FP6 Marie-Curie research Training Network "Constellation: the origin of stellar masses" (MRTN-CT-2006-035890). R.S.F. is supported by a Grant-in-Aid from the Ministry of Education, Culture, Sports, Science and Technology of Japan (No. 20749113).

## References


Anglada, G., Estalella, R., Pastor, F., Rodríguez, L. F., & Haschick, A. 1996, ApJ, 463, 205
Becker, R. H., White, R. L., Helfand, D. J., & Zoonematkermani, S. 1994, ApJS, 91, 347
Beltrán, M. T., Cesaroni, R., Neri, R., et al. 2004, ApJ, 601, L187
Beltrán, M. T., Cesaroni, R., Neri, R., et al. 2005, A&A, 435, 901
Beltrán, M. T., Cesaroni, R., Codella, C., et al. 2006, Nature, 443, 427
Beuther, H., Churchwell, E. B., McKee, C. F., & Tan, J. C. 2007, in Protostars and Planets V, ed. B. Reipurth, D. Jewitt, & K. Keil (Tucson: Univ. Arizona Press), 165
Bonnell, I. A., & Bate, M. R. 2005, MNRAS, 362, 915
Bonnell, I. A., Larson, R. B., & Zinnecker, H. 2007, in Protostars and Planets V, ed. B. Reipurth, D. Jewitt, & K. Keil (Tucson: Univ. Arizona Press), 149
Brand, J. 1986, Ph.D. Thesis, Leiden University
Bronfan, L., Nyman, L.-Å, & May, J. 1996, A&AS, 115, 81
Cesaroni, R., Walmsley, C. M., & Churchwell, E. 1992, A&A, 256, 618
Cesaroni, R., Churchwell, E., Hofner, P., Walmsley, C. M., & Kurtz, S. 1994, A&A, 288, 903
Cesaroni, R., Codella, C., Furuya, R. S., & Testi, L. 2003, A&A, 401, 227
Cesaroni, R., Neri, R., Olmi, L., et al. 2005, A&A, 434, 1039
Codella, C., Testi, L., & Cesaroni, R. 1997, A&A, 325, 282 (Paper I)
De Buizer, J. M. 2006, ApJ, 642, L57
Dent, W. R. T., Little, L. T., & White, G. J. 1984, MNRAS, 210, 173
Forster, J. R., & Caswell, J. L. 1989, ApJ, 530, 371
Forster, J. R., & Caswell, J. L. 1999, A&AS, 137, 43
Forster, J. R., & Caswell, J. L. 2000, A&A, 213, 339
Fuller, G. A., Zijlstra, A. A., & Williams, S. J. 2001, ApJ, 555, 125
Furuya, R. S., Cesaroni, R., Codella, C., et al. 2002, A&A, 390, L1
Gibb, A. G., Hoare, M. G., Little, L. T., & Wright, M. C. H. 2003, MNRAS, 339, 1011
Hatchell, J., Fuller, G. A., Millar, T. J., Thompson, M. A., & Macdonald, G. H. 2000, A&A, 357, 637
Hoare, M. G., Kurtz, S. E., Keto, E., & Hofner, P. 2007, in Protostars and Planets V, ed. B. Reipurth, D. Jewitt, & K. Keil (Tucson: Univ. Arizona Press), 181
Hofner, P., & Churchwell, E. 1996, A&AS, 120, 283
Hunter, T. R., Churchwell, E., Watson, C., et al. 2000, AJ, 119, 271
Kurtz, S., Cesaroni, R., Churchwell, E., Hofner, P., & Walmsley, C. M. 2000, in Protostars and Planets IV, ed. V. Mannings, A. P. Boss, & S. S. Russell (Tucson: Univ. Arizona Press), 299
Little, L. T., Kelly, M. L., & Murphy, B. T. 1998, MNRAS, 294, 105
López-Sepulcre, A., Codella, C., Cesaroni, R., Marcelino, N., & Walmsley, C.M. 2009, A&A, 499, 811
MacLaren, I., Richardson, K. M., & Wolfendale, A. W. 1998, ApJ, 333, 821
Olmi, L., Cesaroni, R., & Walmsley, C. M. 1993, A&A, 276, 489
Palla, F., & Stahler, S. 1993, ApJ, 418, 414
Panagia, N. 1973, AJ, 78, 929
Plume, R., Jaffe, D. T., & Evans II, N. J. 1992, ApJS, 78, 505
Schraml, J., & Mezger, P. G. 1969, ApJ, 156, 269
Shepherd, D. S., Churchwell, E., & Wilner, D. J. 1997, ApJ, 482, 355
Stahler, S., Palla, F., & Ho, P. T. P. 2000, in Protostars and Planets IV, ed. V. Mannings, A. P. Boss, & S. S. Russell (Tucson: Univ. Arizona Press), 327
Ungerechts, H., Walmsley, C. M., & Winnewisser, G. 1986, A&A, 157, 207
van Dishoek, E. F., & Blake, G. A. 1998, ARA&A, 36, 317
Walsh, A. J., Hyland, A. R., Robinson, G., & Burton, M. G. 1997, MNRAS, 291, 261
Walsh, A. J., Burton, M. G., Hyland, A. R., & Robinson, G. 1998, MNRAS, 301, 640
Walsh, A. J., Bertoldi, F., Burton, M. G., & Nikola, T. 2001, 326, 36
Walsh, A. J., Macdinald, G. H., Alvey, N. D. S., Burton, M. G., & Lee, J.-K. 2003, A&A, 410, 597
Wolfire, M. G., & Cassinelli, J. P. 1987, ApJ, 319, 850
Zhang, B., Zheng, X. W., Reid, M. J., et al. 2009, ApJ, 693, 419